Positioning-Aided Channel Estimation for Multi-LEO Satellite Cooperative Beamforming

N.B. When citing this work, cite the original published paper.

(article starts on next page)

Positioning-Aided Channel Estimation for Multi-LEO Satellite Cooperative Beamforming

Yuchen Zhang, Pinjun Zheng, Jie Ma, Henk Wymeersch, *Fellow, IEEE*, and Tareq Y. Al-Naffouri, *Fellow, IEEE*

Abstract—We investigate a multi-low Earth orbit (LEO) satellite system that simultaneously provides positioning and communication services to terrestrial user terminals. To address the challenges of accurately acquiring channel state information in LEO satellite systems, we propose a novel two-timescale positioning-aided channel estimation framework, exploiting the distinct variation rates of position-related parameters and channel gains inherent in LEO satellite channels. Using the misspecified Cramér-Rao bound (MCRB) theory, we systematically analyze positioning performance under practical imperfections, such as inter-satellite clock bias and carrier frequency offset. Furthermore, we theoretically demonstrate how position information derived from downlink positioning can enhance uplink channel estimation accuracy, even in the presence of positioning errors, through an MCRB-based analysis. To address the limited link budgets and communication rates of single-satellite communication, we develop a multi-LEO cooperative beamforming strategy for downlink transmission that leverages cluster-wise satellite cooperation while maintaining reduced complexity. Theoretical analyses and numerical results confirm the effectiveness of the proposed framework in facilitating high-precision downlink positioning under practical imperfections, facilitating uplink channel estimation, and enabling efficient downlink communication.

Index Terms—LEO satellite positioning and communication, channel estimation, MCRB, cooperative beamforming.

I. INTRODUCTION

The evolution of mobile communications has been driven by a remarkable vision: enabling seamless, high-speed information access from any point on Earth. While generational advances in cellular networks, from 1G to 5G and beyond, have largely achieved this goal in urban and suburban areas where infrastructure deployment is economically viable, significant challenges remain in rural and remote regions. In these underdeveloped areas, reliable communication and internet access often remain either unavailable or prohibitively expensive, contributing to a growing digital divide [1]. The non-terrestrial

networks (NTN)-based communications have emerged as a promising solution to bridge global connectivity gaps, leveraging airborne and spaceborne platforms, such as high-altitude platforms (HAPs) and satellites, as aerial access points [2]–[7]. Among these platforms, low Earth orbit (LEO) satellites have garnered particular attention due to several advantages over medium Earth orbit (MEO), geostationary Earth orbit (GEO) satellites, and HAPs. These advantages include lower path loss and reduced propagation delays, increased flexibility in constellation design, and comparatively lower deployment and launch costs [8]–[10].

The advancement of LEO satellite-based global connectivity presents promising opportunities alongside significant challenges, particularly in channel estimation, a crucial aspect for meeting increasingly demanding high-speed communication requirements [11], [12]. While receivers can effectively mitigate channel aging by compensating for Doppler shift caused by rapid LEO satellite movement [8], [11], [13], the substantial propagation distance compared to terrestrial networks results in severe signal power attenuation. This attenuation particularly impacts pilot-based channel estimation methods, which struggle with low receive power, making effective channel state information (CSI) acquisition challenging, especially for power-constrained user terminals (UTs) such as mobile devices in the uplink. On the other hand, despite the reduced orbital altitude compared to MEO and GEO satellites, LEO communication links still span distances vastly exceeding typical terrestrial communication counterparts. This extended signal travel distance, combined with limited onboard power resources, significantly constrains the link budget of single-LEO satellite-based communication systems, creating a substantial barrier to achieving the ambitious throughput goals of wideband NTN communications [2], [12], [14].

Although satellite channels pose significant challenges for CSI acquisition, they exhibit distinct characteristics compared to terrestrial channels, particularly strong line-of-sight (LOS) dominance and pronounced geometric structures [14]. These properties are intrinsically tied to position information [10], suggesting that judicious use of UT position knowledge could help alleviate channel estimation challenges in LEO satellite communications, e.g., by enabling partial channel inference through the reconstruction of geometry-dependent components such as steering vectors. This viewpoint naturally raises two key questions: *(i)* how to acquire accurate UT position information efficiently in LEO satellite networks, and *(ii)* how to leverage such information to improve LEO channel estimation and,

ultimately, communication performance. On the other hand, to overcome the limited link budget inherent in single-satellite service, multi-satellite cooperative transmission has emerged as a promising solution under diverse design objectives [15]–[24]. Recent works have, for example, designed cooperative transmission schemes to proactively mitigate asynchronous interference in single-carrier/statistical-CSI settings [22], extended such treatments to orthogonal frequency division multiplexing (OFDM) systems (often resorting to high-complexity quadratically constrained quadratic program (QCQP)-based formulations) [23], or emphasized joint power allocation and user scheduling with heuristic precoder constructions [24]. While these advances are highly relevant, they are not directly aligned with the objective of this paper, which uses cooperative beamforming primarily as a controlled baseline to assess the utility of positioning-aided CSI. Moreover, despite the growing interest in multi-satellite cooperation, the *computational scalability* of cooperative beamforming remains a key bottleneck, especially for resource-constrained LEO satellite platforms.

The role of position information in terrestrial networks has been widely recognized for enhancing communication performance [25]–[29]. For instance, [25] introduces location awareness in 5G networks, demonstrating its potential for synchronizing coordinated communication schemes. Similarly, [26] showcases how position information facilitates beam alignment in millimeter-wave communication. These approaches typically rely on position information from either global navigation satellite system (GNSS) [25], [26] or radio sensing [27]–[29]. However, in LEO satellite scenarios, obtaining position information of terrestrial UTs through radar-like sensing at LEO satellites becomes impractical due to excessive round-trip signal attenuation. While GNSS appears to be a viable alternative, as demonstrated in [24], where UTs' positions are obtained via GNSS and fed back to LEO satellites for downlink communication, the critical impact of positioning errors and the reliance on overidealistic synchronization assumptions remains under-explored and warrant further investigation in practical implementations.

Concurrent with advances in LEO satellite communication, there is growing interest in exploring LEO satellites as potential supplements or alternatives to GNSS [30]–[34]. This interest arises from the inherent advantages of LEO satellites over GNSS, including stronger signal reception, extensive constellations, and broad frequency diversity, characteristics that have also partially driven the success of LEO satellite communications [31], [35], [36]. Recent research has begun to investigate the integration of LEO satellite communication and positioning functionalities. For instance, [37] proposes a massive multi-input-multi-output (MIMO) LEO satellite system that supports simultaneous communication and positioning in the downlink, designing hybrid beamforming to meet their distinct requirements. However, this work primarily focuses on the tradeoff between positioning and communication performance, overlooking their mutual benefits such as the potential of positioning in facilitating channel estimation, which is

a critical challenge in LEO satellite systems. Moreover, it does not account for the inevitable clock bias and carrier frequency offset (CFO) among LEO satellites, factors that may significantly affect positioning performance.

In this paper, we investigate a cluster of LEO satellites, each equipped with a uniform planar array (UPA), that simultaneously provide downlink positioning and communication services to multiple single-antenna terrestrial UTs. We aim to address the key challenges that specifically arise in this setting: characterizing positioning performance under practical synchronization imperfections such as inter-satellite clock bias and CFO; leveraging user position information to enhance channel estimation while accounting for inevitable positioning errors; and mitigating single-satellite link-budget limitations through a carefully designed cooperative multi-satellite beamforming scheme with reduced optimization complexity.

The main contributions of this paper are as follows.

- Building on the distinct variation rates of position-related parameters and random channel gains in LEO satellite channels, as detailed in Section II, we propose an innovative two-timescale frame structure. Downlink positioning operates on the longer position-coherent timescale, while uplink channel estimation and downlink communication occur on the shorter channel gain-coherent timescale. Through this framework, each process is scheduled according to its variation rate, maximizing resource utilization while preserving the potential to leverage positioning for efficient channel estimation and communication.

- To move beyond idealized synchronization assumptions commonly adopted in prior works, we extend the use of the misspecified Cramér-Rao bound (MCRB) framework to explicitly capture the impact of inter-satellite clock bias and CFO. Unlike the classical Cramér-Rao bound (CRB), the MCRB is designed for estimation under model mismatch [38]. Through this lens, we rigorously quantify how these synchronization-related impairments distort time-of-arrival (TOA) and Doppler measurements and, in turn, degrade positioning accuracy in practical LEO scenarios.

- Within the proposed positioning-aided channel estimation (PACE) framework, we show how large-timescale positioning errors propagate into small-timescale channel estimation, creating inherent model mismatch. By applying the MCRB, we systematically analyze how uncertainty in the positioning stage translates into performance loss in uplink channel estimation, thereby identifying the robustness margins required for practical position-aided designs.

- We propose a cooperative beamforming baseline for downlink communication, where each UT is simultaneously served by all LEO satellites in a cluster. We adopt the weighted minimal mean squared error (WMMSE) framework and develop a low-complexity solution that strategically exploits block coordinate descent (BCD), strong duality, and matrix-inversion structures to mitigate the otherwise prohibitive computational burden of multi-satellite cooperation. Importantly, this baseline is
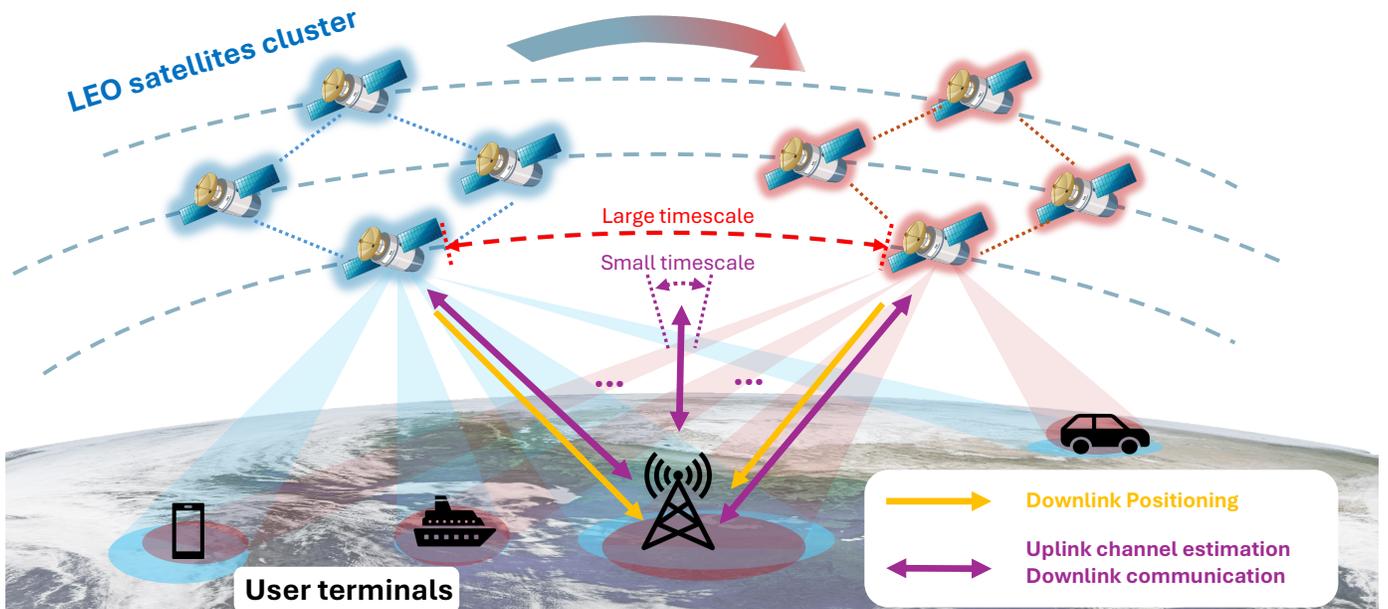
Fig. 1. A cluster of LEO satellites traverses orbit while simultaneously delivering positioning and communication services to UTs. Each UT is served by all LEO satellites within the cluster for both functionalities. Positioning operations in the downlink occur over a relatively large timescale, whereas uplink channel estimation and downlink communication are carried out on a smaller timescale. The specific definitions of these timescales will be clarified later.

designed to be computationally practical and to enable a transparent evaluation of the proposed PACE framework by comparing the performance achieved under nominal (PACE-estimated) versus ground-truth channel models.

This paper is structured as follows. We begin by presenting the system model in Section II. Section III examines both downlink positioning and uplink channel estimation performance through MCRB theory, incorporating the PACE. A cooperative beamforming approach for downlink communications is detailed in Section IV. Numerical results are presented in Section V, with conclusions drawn in Section VI.

Notations: Scalars are written in regular lowercase, while vectors and matrices are denoted by bold lowercase and bold uppercase letters, respectively. For a vector $\mathbf{a}$, its 2-norm is expressed as $\|\mathbf{a}\|$. We use T and H as superscripts to indicate transpose and Hermitian transpose operations. For a matrix $\mathbf{A}$, $\mathrm{Tr}(\mathbf{A})$ represents its trace. Complex numbers are handled by $\Re\{a\}$ and $\Im\{a\}$ for their real and imaginary components. A block-diagonal matrix constructed from matrices $\mathbf{A}_1, \ldots, \mathbf{A}_N$ is written as $\mathrm{blkdiag}\{\mathbf{A}_1, \ldots, \mathbf{A}_N\}$. The Kronecker product is symbolized by $\otimes$. For statistical distributions, $\mathcal{CN}(\boldsymbol{\mu}, \mathbf{C})$ represents a circularly symmetric complex Gaussian distribution characterized by mean $\boldsymbol{\mu}$ and covariance matrix $\mathbf{C}$.

II. SYSTEM MODEL

As illustrated in Fig. 1, we consider a scenario where a cluster of S LEO satellites serves U UTs, simultaneously providing downlink positioning and communication services. In this paper, we assume that no handovers occur during operation. The impact of both intra- and inter-cluster handovers is left for future investigation. Each LEO satellite is equipped with a UPA comprising $N = N_{\mathrm{h}} \times N_{\mathrm{v}}$ half-wavelength-spaced

antennas, where N_{h} and N_{v} denote the numbers of antennas in the horizontal and vertical dimensions, respectively. Each UT is equipped with a single antenna.[1] While accurate CSI is essential for achieving efficient downlink communication, channel estimation is challenging in space-borne communication systems due to the limited link budget and short coherence time. These challenges originate from the long travel distance between the satellites and the UTs as well as the high-speed satellite movement [12]. In the following, we first introduce the adopted channel model. Subsequently, we elaborate on a two-timescale property of this model, which can be leveraged to facilitate efficient channel acquisition at LEO satellites, thereby enhancing downlink communications. Note that handovers in LEO satellite systems typically occur on the order of tens of seconds to a few minutes, and thus span multiple position-coherent large-timescale frames (see further discussion later). Since the proposed PACE framework focuses on the integration of positioning and communication *within* each frame, we omit explicit handover modeling to avoid introducing an additional control-plane layer and associated redundancy beyond the scope of this work. This simplifying assumption is also widely adopted in prior studies such as [15], [16], [19], [24].

A. Channel Model

We consider a satellite communication system operating at relatively high-frequency bands such as the Ku and Ka bands,

---

[1]Note that extending single-antenna UTs to multi-antenna setting is a promising direction: receiver spatial resolution can help separate signals with distinct Dopplers and delays and mitigate asynchronous interference [23]. However, a rigorous treatment would also require modifying the positioning model to incorporate array orientation and angle-related measurements, which is beyond the present scope and will be pursued in future work.

where the channel is dominated by LOS propagation [14], [18].[2] Assume the system employs the OFDM scheme with K subcarriers. Let $\Delta f = B/K$ and $T = 1/\Delta f$ denote the subcarrier spacing and symbol duration, respectively, where B is the signal bandwidth. The channel from the s-th LEO satellite to the u-th UT during the ℓ-th OFDM symbol over the k-th subcarrier is expressed as[3]

$$\mathbf{h}_{s,u}[\ell,k] = \alpha_{s,u} G\left(\theta_{s,u}^{\mathrm{el}}\right) e^{\jmath 2\pi(\ell T \upsilon_{s,u} - k\Delta f \tau_{s,u})} \mathbf{a}\left(\boldsymbol{\theta}_{s,u}\right), \quad (1)$$

where $\alpha_{s,u}$ is the complex channel gain, $G(\cdot)$ is the symmetric antenna radiation pattern determined solely by the elevation angle [39], $\tau_{s,u}$ and $\upsilon_{s,u}$ represent the TOA and Doppler shift, respectively, and $\mathbf{a}(\boldsymbol{\theta}_{s,u}) \in \mathbb{C}^N$ is the steering vector at the LEO satellite, with $\boldsymbol{\theta}_{s,u} = [\theta_{s,u}^{\mathrm{az}}, \theta_{s,u}^{\mathrm{el}}]^{\mathsf{T}}$ being the angle-of-departure (AOD) composed of both azimuth and elevation angles. Without loss of generality, we assume the UPA at each satellite is deployed on the XY-plane of its local coordinate system. Hence, the steering vector can be expressed as

$$\mathbf{a}\left(\boldsymbol{\theta}_{s,u}\right) = e^{-\jmath 2\pi \phi_{s,u}^{\mathrm{h}} \mathbf{n}(N_{\mathrm{h}})} \otimes e^{-\jmath 2\pi \phi_{s,u}^{\mathrm{v}} \mathbf{n}(N_{\mathrm{v}})}, \quad (2)$$

where $\mathbf{n}(N) = [0, \ldots, N-1]^{\mathsf{T}}$, $\phi_{s,u}^{\mathrm{h}} = d \cos\theta_{s,u}^{\mathrm{az}} \cos\theta_{s,u}^{\mathrm{el}}/\lambda$, and $\phi_{s,u}^{\mathrm{v}} = d \sin\theta_{s,u}^{\mathrm{az}} \cos\theta_{s,u}^{\mathrm{el}}/\lambda$. Here, d denotes the antenna spacing along each dimension, and λ is the wavelength at the central carrier frequency f_c.

The complex channel gain can be modeled as

$$\alpha_{s,u} = e^{\jmath \psi_{s,u}} \beta_{s,u}, \quad (3)$$

where $\psi_{s,u}$ represents the random phase difference between the transmitter and receiver [40], and $\beta_{s,u}$ denotes the path loss incorporating both the large-scale path losses and small-scale fading, as described in [41]. Specifically, the path loss $\beta_{s,u}$, in the dB domain, is characterized as

$$-20\log_{10}\beta_{s,u} = \beta_{s,u}^{\mathrm{FS}} + \beta_{s,u}^{\mathrm{SF}} + \beta_{s,u}^{\mathrm{CL}} + \beta_{s,u}^{\mathrm{AB}} + \beta_{s,u}^{\mathrm{SC}} \text{ [dB], } (4)$$

where $\beta_{s,u}^{\mathrm{FS}}$ denotes the free-space path loss, $\beta_{s,u}^{\mathrm{SF}}$ accounts for shadow fading modeled as a Gaussian random variable, $\beta_{s,u}^{\mathrm{CL}}$ represents the clutter loss, $\beta_{s,u}^{\mathrm{AB}}$ captures atmospheric absorption effects, and $\beta_{s,u}^{\mathrm{SC}}$ accounts for attenuation caused by ionospheric or tropospheric scintillation.

B. Timescale Analysis and Frame Structure

1) Timescale Analysis: From (1), we observe that the LEO satellite channel is governed by two categories of parameters:

- *Large-Timescale Parameters:* These parameters are associated with the positions of the satellites and UTs, and include the Doppler shift, TOA, and AOD. Although LEO satellites move rapidly, their orbits are *predictable* and well-determined. Thus, the dominant deterministic Doppler component evolves coherently with other geometry-related parameters such as TOA and AOD.

---

[2]While the multipath effect can still play a significant role in dense urban environments, LEO satellite communications are primarily designed to serve suburban, rural, and remote areas, such as oceans and deserts, where terrestrial infrastructure is sparse or nonexistent, and scatterers are greatly reduced. Consequently, LOS propagation becomes even more dominant.

[3]Note that, though not further indexed for symbolic simplicity, this expression is viewed within one channel-gain coherent interval (as elaborated later) and $\upsilon_{s,u}$, $\tau_{s,u}$, and $\boldsymbol{\theta}_{s,u}$ are viewed constant for many such intervals.
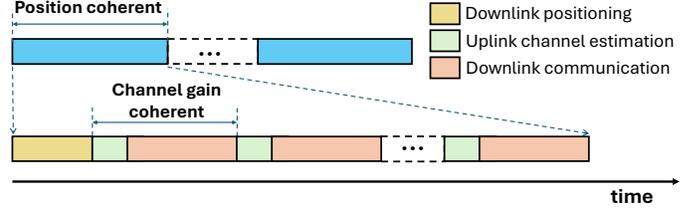

Fig. 2. Illustration of the two-timescale frame structure, where each large-timescale frame encompasses multiple small-timescale subframes. The large-timescale frame is governed by the position-coherent time, while the small-timescale subframe is defined by the channel gain-coherent time.

As long as the UTs' positions do not change abruptly (which is typically the case in practice), this predictability remains valid over the position-coherent timescale, which is primarily governed by the update rate of the UTs' positions rather than the satellites' trajectories. Therefore, it is reasonable to assume that large-timescale parameters vary on the order of seconds or longer in typical scenarios.

- *Small-Timescale Parameters:* These parameters consist of random variations in the amplitude and phase of the channel gain. Residual Doppler fluctuations that remain after compensation, due to estimation errors, are also absorbed into this category. Unlike the geometry-determined large-timescale parameters, these small-timescale effects are inherently unpredictable and fluctuate rapidly. Such variations can arise from tropospheric scintillation, which induces sub-second fluctuations in Ka-band LEO satellite channels depending on atmospheric and orbital conditions [42]. Moreover, even though the LOS component dominates at Ku/Ka bands, nearby mobile scatterers can still generate multipath components that merge with the LOS path, forming a composite channel gain that exhibits small-scale fading with amplitude and phase variations on millisecond timescales [18], [28].

Note that a similar dual-timescale effect has been analyzed and exploited in terrestrial systems [27], [43]. In LEO satellite channels, the Doppler shift induced by the high-speed motion of the satellite causes rapid temporal phase rotations. While this effect can be largely mitigated by carrier synchronization at the receiver, small residual errors may remain [8], limiting its impact on communication performance. Nevertheless, we retain the Doppler shift in the channel model since it also provides a valuable measurement for positioning, as will be discussed later. For positioning, the Doppler shift must be explicitly estimated prior to being compensated for communication purposes.

2) Two-Timescale Frame Structure: Inspired by the timescale analysis, we propose a two-timescale frame structure that exploits the inherent two-timescale property of LEO channels to enable efficient channel estimation/reconstruction, thus facilitating downlink LEO transmission. As shown in Fig. 2, the duration of a large-timescale frame is determined by the position-coherent time, which indicates the interval after which the UTs' position information becomes outdated. Each large-timescale frame begins with an initial subframe for downlink

positioning, where UTs' position estimates can be fed back to LEO satellites [24], [44], followed by multiple small-timescale subframes during which the channel gain remains coherent. We would like to emphasize that the feedback carries only low-rate UT position information (a 3D real vector) that remains coherent over the large-timescale interval. This leads to negligible overhead and no stringent latency requirements. Moreover, the dominant uncertainty is the position estimation error (already modeled in our analysis), under which Fig. 5 shows that PACE-based channel reconstruction is robust in practical regimes. Therefore, explicit feedback-link errors are omitted. Note that time division duplex (TDD)[4] is adopted to differentiate between uplink and downlink transmissions. The proposed approach leverages uplink-downlink channel reciprocity, which applies uplink channel estimation to optimize downlink communication design.

To further substantiate the fundamental rationales behind the proposed structure for LEO downlink communications, we highlight its potential advantages by comparing it with positioning-free uplink channel estimation protocols, where the channel is directly estimated at the LEO satellites using uplink pilots without requiring position information from UTs [11], [13]. This approach involves estimating an unknown channel vector/matrix, which can incur significant pilot overhead, especially when large antenna arrays are employed. With the proposed position information-aided framework, vector-type channel estimation can be transformed into scalar-type estimation by exploiting the channel structure. This transformation offers the potential for higher channel estimation accuracy with the same pilot overhead. Alternatively, to achieve equivalent channel estimation accuracy, reduced pilot overhead is required, thus preserving more resources for data transmission.

In the following, we will first conduct a performance analysis based on the two-timescale PACE and then propose a cooperative beamforming method across multiple LEO satellites for downlink communication.

III. TWO-TIMESCALE POSITIONING-AIDED CHANNEL ESTIMATION

To characterize its performance limits, we conduct a two-phase theoretical performance analysis[5] for PACE. In the first phase, we analyze the downlink multi-LEO satellite-based positioning performance, while in the second phase, we assess the uplink channel estimation performance.

Note that model mismatches can arise from various hardware imperfections.[6] First, clock biases are inevitable between satellites and UTs as well as among satellites themselves. Although sub-nanosecond synchronization can be achieved by equipping LEO satellites with GNSS receivers [48], the received signals remain subject to ionospheric and tropospheric delays during propagation [49]. These delays, shaped by temperature, pressure, humidity, and the satellite's elevation angle relative to the UT, induce unique offsets for each satellite–UT pair and effectively translate into *equivalent* clock biases in the signal model. Second, low-cost oscillators and inherent hardware impairments can introduce CFO [50]. Many localization algorithms simplify the underlying model by neglecting certain factors to reduce analytical complexity. To capture the impact of this simplification, in the positioning phase we employ a simplified model to estimate unknowns that are actually generated by a more realistic one, which inherently introduces model mismatches. Similarly, in the second phase, position information-aided channel estimation, estimation errors in UT positions also lead to mismatches. Consequently, the performance bounds under such conditions can be effectively characterized using the MCRB [38], [51].

A. Large-Timescale Downlink Positioning

1) Signal Model: Let $\mathbf{t}_s[\ell, k] \in \mathbb{C}^U$ be the pilot (with unit-modulus elements) sent by the s-th LEO satellite over the ℓ-th symbol and the k-th subcarrier. We assume the satellites are multiplexed in the positioning phase through time-division multiple access (TDMA) [36]. The received baseband signal at the u-th UT, from the s-th satellite can be expressed as

$$y_{s,u}[\ell, k] = \mathbf{h}_{s,u}^{\mathsf{T}}[\ell, k] \mathbf{F}_s \mathbf{t}_s[\ell, k] + z_u[\ell, k]$$
$$= \vartheta_{s,u} \gamma[\ell, k] \mathbf{a}^{\mathsf{T}}(\boldsymbol{\theta}_{s,u}) \mathbf{f}_s[\ell, k] + z_u[\ell, k], \quad (5)$$

where $\vartheta_{s,u} = \alpha_{s,u} G(\theta_{s,u}^{\mathrm{el}})$, $\gamma[\ell, k] = e^{j2\pi(\ell T v_{s,u} - k\Delta f \tau_{s,u})}$, $\mathbf{f}_s[\ell, k] = \mathbf{F}_s \mathbf{t}_s[\ell, k]$ with $\mathbf{F}_s \in \mathbb{C}^{N \times U}$ being the beamforming matrix, and $z_u[\ell, k] \sim \mathcal{CN}(0, N_0 \Delta f)$ is the additive white Gaussian noise (AWGN) with single-side power spectral density (PSD) N_0. Without loss of generality, the following derivation focuses on the u-th UT.

Let $\boldsymbol{\eta}_{s,u} = [\acute{\boldsymbol{\eta}}_{s,u}^{\mathsf{T}}, \dot{\boldsymbol{\eta}}_{s,u}^{\mathsf{T}}]^{\mathsf{T}} \in \mathbb{R}^6$ denote the unknown channel-domain parameters in the signal received from the s-th satellite, where $\acute{\boldsymbol{\eta}}_{s,u} = [v_{s,u}, \tau_{s,u}]^{\mathsf{T}} \in \mathbb{R}^2$ are the parameters used for UT positioning, and $\dot{\boldsymbol{\eta}}_{s,u} = [\boldsymbol{\theta}_{s,u}^{\mathsf{T}}, \Re(\vartheta_{s,u}), \Im(\vartheta_{s,u})]^{\mathsf{T}} \in \mathbb{R}^4$ are treated as nuisance parameters. Delay $\tau_{s,u}$ and Doppler $v_{s,u}$ are directly determined by the UT's position and velocity relative to the satellites, making them the most reliable observables for positioning. In contrast, the AOD $\boldsymbol{\theta}_{s,u}$ is not exploited here due to the limited angular resolution of LEO satellites operating at high altitudes, which makes AOD estimates unreliable unless extremely large arrays are employed. Similarly, the channel

gain $\vartheta_{s,u}$ is heavily influenced by environmental variability and hardware impairments and thus provides little stable geometric information for positioning, except in fingerprinting-based approaches [40].

We further concatenate all the utilized channel-domain parameters collected from S satellites as $\acute{\boldsymbol{\eta}}_u = [\acute{\boldsymbol{\eta}}_{1,u}^{\mathsf{T}}, \ldots, \acute{\boldsymbol{\eta}}_{S,u}^{\mathsf{T}}]^{\mathsf{T}} \in \mathbb{R}^{2S}$. Therefore, in the large-timescale downlink positioning, we first estimate $\acute{\boldsymbol{\eta}}_u$ based on $y_{s,u}[\ell,k]$, $s = 1,\ldots,S$, $\ell = 1,\ldots,L_{\mathrm{p}}$, $k = 1,\ldots,K$, where L_{p} denotes the number of pilot symbols for downlink positioning. Afterwards, we estimate the u-th UT's position, clock biases, and CFOs.

2) The FIM of $\boldsymbol{\eta}_{s,u}$: Let $\mu_{s,u}[\ell,k]$ denote the noise-free version of $y_{s,u}[\ell,k]$ and $\mathbf{G}_{s,u}[\ell,k] = [\mathbf{g}_v[\ell,k], \mathbf{g}_\tau[\ell,k], \mathbf{g}_{\theta_{\mathrm{az}}}[\ell,k], \mathbf{g}_{\theta_{\mathrm{el}}}[\ell,k], \mathbf{g}_{\vartheta,\mathrm{R}}[\ell,k], \mathbf{g}_{\vartheta,\mathrm{I}}[\ell,k]] \in \mathbb{C}^{N \times 6}$. Here, the columns fulfill

$$\mathbf{g}_v[\ell,k] = \vartheta_{s,u}\gamma[\ell,k](\jmath 2\pi \ell T)\mathbf{a}(\boldsymbol{\theta}_{s,u}), \tag{6a}$$

$$\mathbf{g}_\tau[\ell,k] = \vartheta_{s,u}\gamma[\ell,k](-\jmath 2\pi k\Delta f)\mathbf{a}(\boldsymbol{\theta}_{s,u}), \tag{6b}$$

$$\mathbf{g}_{\theta_{\mathrm{az}}}[\ell,k] = \vartheta_{s,u}\gamma[\ell,k]\frac{\partial \mathbf{a}(\boldsymbol{\theta}_{s,u})}{\partial \theta_{s,u}^{\mathrm{az}}}, \tag{6c}$$

$$\mathbf{g}_{\theta_{\mathrm{el}}}[\ell,k] = \vartheta_{s,u}\gamma[\ell,k]\frac{\partial \mathbf{a}(\boldsymbol{\theta}_{s,u})}{\partial \theta_{s,u}^{\mathrm{el}}}, \tag{6d}$$

$$\mathbf{g}_{\vartheta,\mathrm{R}}[\ell,k] = \gamma[\ell,k]\mathbf{a}(\boldsymbol{\theta}_{s,u}), \tag{6e}$$

$$\mathbf{g}_{\vartheta,\mathrm{I}}[\ell,k] = \jmath\gamma[\ell,k]\mathbf{a}(\boldsymbol{\theta}_{s,u}). \tag{6f}$$

Based on the signal received from the s-th satellite, the Fisher information matrix (FIM) of $\boldsymbol{\eta}_{s,u}$ can be computed by the Slepian-Bangs formula as

$$\mathbf{J}_s(\boldsymbol{\eta}_{s,u})$$
$$= \frac{2}{N_0 \Delta f} \sum_{\ell=1}^{L_{\mathrm{p}}} \sum_{k=1}^{K} \Re\left\{\left(\frac{\partial \mu_{s,u}[\ell,k]}{\partial \boldsymbol{\eta}_{s,u}}\right)\left(\frac{\partial \mu_{s,u}[\ell,k]}{\partial \boldsymbol{\eta}_{s,u}}\right)^{\mathsf{H}}\right\}, \tag{7}$$
$$= \frac{2}{N_0 \Delta f} \sum_{\ell=1}^{L_{\mathrm{p}}} \sum_{k=1}^{K} \Re\left\{\mathbf{G}_{s,u}^{\mathsf{T}}[\ell,k]\mathbf{f}_s[\ell,k]\mathbf{f}_s[\ell,k]^{\mathsf{H}}\mathbf{G}_{s,u}^{*}[\ell,k]\right\}.$$

3) The FIM of $\acute{\boldsymbol{\eta}}_u$: Partitioning $\mathbf{J}_s(\boldsymbol{\eta}_{s,u}) = [\mathbf{X}, \mathbf{Y}; \mathbf{Y}^{\mathsf{T}}, \mathbf{Z}]$, where $\mathbf{X} \in \mathbb{R}^{2\times 2}$, we can compute the FIM of the total utilized channel-domain parameters $\acute{\boldsymbol{\eta}}_{s,u}$ as $\mathbf{J}_s(\acute{\boldsymbol{\eta}}_{s,u}) = \mathbf{X} - \mathbf{Y}\mathbf{Z}^{-1}\mathbf{Y}^{\mathsf{T}}$. Then, we can obtain the FIM of $\acute{\boldsymbol{\eta}}_u$ as

$$\mathbf{J}(\acute{\boldsymbol{\eta}}_u) = \mathrm{blkdiag}\{\mathbf{J}_1(\acute{\boldsymbol{\eta}}_{1,u}), \ldots, \mathbf{J}_S(\acute{\boldsymbol{\eta}}_{S,u})\}. \tag{8}$$

Based on this, we can infer that the achievable lowest estimation error on $\acute{\boldsymbol{\eta}}_u$ regardless of the adopted algorithms is characterized by the Gaussian distribution $\mathcal{N}(\mathbf{0}, \mathbf{J}^{-1}(\acute{\boldsymbol{\eta}}_u))$. Any algorithm achieving this error covariance matrix is called an *efficient estimator*.

4) MCRB and LB Derivation: Suppose an efficient estimator is utilized to estimate $\acute{\boldsymbol{\eta}}_u$. We now focus on estimating the position-domain parameters, where the aforementioned model mismatches occur. We consider a scenario where each satellite-UT pair has a distinct clock bias $b_{s,u}$ and CFO $\delta_{s,u}$. For convenience, we use b_u and δ_u to denote an average clock bias and CFO among the S satellites, thus we can rewrite these individual clock biases and CFOs as $b_{s,u} = b_u + \Delta b_{s,u}$

and $\delta_{s,u} = \delta_u + \Delta\delta_{s,u}$, respectively, where $\Delta b_{s,u}$ and $\Delta\delta_{s,u}$ denote the differences on each clock bias and CFO.

Let $\mathbf{v}_s \in \mathbb{R}^3$ be the velocity of the s-th LEO satellite. Here, as the velocity of LEO satellite is usually much higher than that of the UT, we ignore the velocity contribution from the UT side. This assumption is justified since LEO satellites move at around 7.6 km/s, whereas UTs typically move at only a few m/s (pedestrians) to a few hundred m/s (vehicles/aircraft), making their velocity contribution two to three orders of magnitude smaller and thus negligible for the Doppler term. Based on the underlying geometric relationship, the forward model between the entries of $\acute{\boldsymbol{\eta}}_u$ and unknown position of the u-th UT can be expressed as

$$\upsilon_{s,u} = \frac{\mathbf{v}_s^{\mathsf{T}}(\mathbf{p}_u - \mathbf{p}_s)}{\lambda\|\mathbf{p}_u - \mathbf{p}_s\|} + \delta_u + \Delta\delta_{s,u} \tag{9}$$

and

$$\tau_{s,u} = \frac{\|\mathbf{p}_u - \mathbf{p}_s\|}{c} + b_u + \Delta b_{s,u}, \tag{10}$$

which we refer to as the *true model*. Here, $\mathbf{p}_u \in \mathbb{R}^3$ and $\mathbf{p}_s \in \mathbb{R}^3$ represent the positions of the u-th UT and the s-th satellite[7], respectively.

In real applications, we often ignore these clock bias and CFO differences, i.e., assuming all satellite-UT pairs have the same clock bias and CFO, for algorithmic simplicity. To account for the impact of such model mismatch, we derive the MCRB, with its fundamentals detailed in Appendix A for completeness. When neglecting the difference on each clock bias and CFO, the *mismatched model* is given by

$$\upsilon_{s,u} = \frac{\mathbf{v}_s^{\mathsf{T}}(\mathbf{p}_u - \mathbf{p}_s)}{\lambda\|\mathbf{p}_u - \mathbf{p}_s\|} + \delta_u \tag{11}$$

and

$$\tau_{s,u} = \frac{\|\mathbf{p}_u - \mathbf{p}_s\|}{c} + b_u. \tag{12}$$

Now, we suppose an estimator that aims to estimate the unknown position of the u-th UT based on the realistic observation $\acute{\boldsymbol{\eta}}_u$ and mismatched model, the total unknown parameters in the mismatch model can be concatenated as $\mathbf{r}_u = [\mathbf{p}_u^{\mathsf{T}}, \delta_u, b_u]^{\mathsf{T}} \in \mathbb{R}^5$. Based on the true model and mismatched model, we can respectively express the true likelihood function ξ_{T} and the mismatched likelihood function ξ_{M} as

$$\xi_{\mathrm{T}}(\acute{\boldsymbol{\eta}}_u; \mathbf{r}_u) \propto e^{(\acute{\boldsymbol{\eta}}_u - \bar{\mathbf{f}}(\mathbf{r}_u))^{\mathsf{T}}\boldsymbol{\Sigma}^{-1}(\acute{\boldsymbol{\eta}}_u - \bar{\mathbf{f}}(\mathbf{r}_u))} \tag{13}$$

and

$$\xi_{\mathrm{M}}(\acute{\boldsymbol{\eta}}_u; \mathbf{r}_u) \propto e^{(\acute{\boldsymbol{\eta}}_u - \tilde{\mathbf{f}}(\mathbf{r}_u))^{\mathsf{T}}\boldsymbol{\Sigma}^{-1}(\acute{\boldsymbol{\eta}}_u - \tilde{\mathbf{f}}(\mathbf{r}_u))}, \tag{14}$$

respectively, where the function $\bar{\mathbf{f}}(\cdot)$ maps $\mathbf{r}_u$ to $\acute{\boldsymbol{\eta}}_u$ according to true model, and the function $\tilde{\mathbf{f}}(\cdot)$ maps $\mathbf{r}_u$ to $\acute{\boldsymbol{\eta}}_u$ according to mismatched model. As mentioned in Section III-A3, $\acute{\boldsymbol{\eta}}_u$ is the estimated channel-domain parameters through an efficient estimator, i.e., $\acute{\boldsymbol{\eta}}_u \sim \mathcal{N}(\bar{\mathbf{f}}(\mathbf{r}_u), \boldsymbol{\Sigma})$, where $\boldsymbol{\Sigma} = \mathbf{J}^{-1}(\acute{\boldsymbol{\eta}}_u)$.

---

[7]Note that LEO satellites' positions are assumed precisely known at the UTs. This information can be obtained from the ephemerides contained in the two-line element files, which are updated daily by the North American Aerospace Defense Command (NORAD) [36].

- *Pseudo-True Parameter:* According to (40), the pseudo-true parameter, denoted by $\tilde{\mathbf{r}}_u$, is given by

$$\tilde{\mathbf{r}}_u = \arg\min_{\mathbf{r}_u} \ \mathcal{D}\big\{\xi_{\mathrm{T}}(\acute{\boldsymbol{\eta}}_u; \bar{\mathbf{r}}_u) \| \xi_{\mathrm{M}}(\acute{\boldsymbol{\eta}}_u; \mathbf{r}_u)\big\}, \qquad (15)$$

$$= \arg\min_{\mathbf{r}_u} \ \big(\bar{\mathbf{f}}(\bar{\mathbf{r}}_u) - \tilde{\mathbf{f}}(\mathbf{r}_u)\big)^{\mathsf{T}} \boldsymbol{\Sigma}^{-1}\big(\bar{\mathbf{f}}(\bar{\mathbf{r}}_u) - \tilde{\mathbf{f}}(\mathbf{r}_u)\big),$$

where the top bar is used to highlight the ground-truth position-domain parameter and forward model. The above problem can be solved using gradient descent with backtracking line search, wherein the true parameters serve as the initial point [52].

- *MCRB:* According to Appendix A, the generalized FIMs, i.e., $\mathbf{A}_{\tilde{\mathbf{r}}_u}$ and $\mathbf{B}_{\tilde{\mathbf{r}}_u}$, can be computed by determining the first- and second-order derivatives of $\tilde{\mathbf{f}}(\mathbf{r}_u)$ with respect to the elements of $\mathbf{r}_u$, as detailed in Appendix B. Subsequently, the MCRB is expressed as

$$\mathrm{MCRB}(\tilde{\mathbf{r}}_u) = \mathbf{A}_{\tilde{\mathbf{r}}_u}^{-1}\mathbf{B}_{\tilde{\mathbf{r}}_u}\mathbf{A}_{\tilde{\mathbf{r}}_u}^{-1}. \qquad (16)$$

- *LB:* Finally, the estimation error lower bound (LB) matrix can be computed as

$$\mathrm{LBM}(\tilde{\mathbf{r}}_u) = \mathrm{MCRB}(\tilde{\mathbf{r}}_u) + \mathrm{Bias}(\tilde{\mathbf{r}}_u), \qquad (17)$$

where $\mathrm{Bias}(\tilde{\mathbf{r}}_u) = (\bar{\mathbf{r}}_u - \tilde{\mathbf{r}}_u)(\bar{\mathbf{r}}_u - \tilde{\mathbf{r}}_u)^{\mathsf{T}}$. Based on (17), the LB for the expected root mean squared error (RMSE) of the u-th UT's position estimation in the presence of model mismatch is given by

$$\mathrm{LB}(\mathbf{p}_u) = \sqrt{\mathrm{Tr}\big([\mathrm{LBM}(\tilde{\mathbf{r}}_u)]_{1:3,1:3}\big)}. \qquad (18)$$

B. Small-Timescale Uplink Channel Estimation

1) Signal Model: After obtaining the positions of UTs, these large-timescale parameters are fed back to the LEO satellites. The second phase of PACE then focuses on estimating the small-timescale parameters (i.e., the channel gains) at the LEO satellites through uplink channel estimation, followed by complete channel reconstruction.

Let $\mathbf{d}_{s,u}[\ell, k] = \mathbf{a}(\boldsymbol{\theta}_{s,u})\sqrt{P_u/K}t_u[\ell, k]$, where P_u denotes the transmit power of the u-th UT, and $t_u[\ell, k]$ represents the unit-modulus pilot transmitted by the u-th UT during the ℓ-th symbol and the k-th subcarrier. Uniform power allocation is employed across all subcarriers. As previously mentioned, the Doppler shift can be largely mitigated in LEO satellite communications. After being exploited in downlink positioning, it is excluded from the signal model including uplink channel estimation and downlink communication for simplicity. Here, we also assume UTs are multiplexed orthogonally using TDMA. By channel reciprocity, the signal received by the s-th LEO satellite from the u-th UT is expressed as

$$\mathbf{y}_{s,u}[\ell, k] = \underbrace{\vartheta_{s,u}e^{-\jmath 2\pi k\Delta f \tau_{s,u}}\mathbf{d}_{s,u}[\ell, k]}_{\bar{\mathbf{g}}_{s,u}[\ell,k]} + \mathbf{z}_s[\ell, k], \qquad (19)$$

where $\mathbf{z}_s[\ell, k] \sim \mathcal{CN}(\mathbf{0}, N_0\Delta f\mathbf{I}_N)$ represents the AWGN.

We observe that $\mathbf{d}_{s,u}[\ell, k]$ is directly determined by the UTs' position feedback. Consequently, instead of estimating the full channel vector, it suffices to estimate only two scalars, i.e., the

channel gain $\vartheta_{s,u}$ and the TOA $\tau_{s,u}$.[8] This significantly simplifies the uplink channel estimation task. However, since the position information is based on estimation rather than ground truth, model mismatch arises again. The received signal based on the estimated position information (mismatched model) is expressed as

$$\mathbf{y}_{s,u}[\ell, k] = \underbrace{\vartheta_{s,u}e^{-\jmath 2\pi k\Delta f \tilde{\tau}_{s,u}}\tilde{\mathbf{d}}_{s,u}[\ell, k]}_{\tilde{\mathbf{g}}_{s,u}[\ell,k]} + \mathbf{z}_s[\ell, k], \qquad (20)$$

where $\tilde{\mathbf{d}}_{s,u}[\ell, k] = \mathbf{a}(\tilde{\boldsymbol{\theta}}_{s,u})\sqrt{P_u/K}t_u[\ell, k]$. Here, $\tilde{\boldsymbol{\theta}}_{s,u}$ represents the calculated angle-of-arrival (AOA) based on the estimated $\tilde{\mathbf{p}}_u$ and the geometrical relationship, given by

$$\tilde{\theta}_{s,u}^{\mathrm{az}} = \mathrm{atan2}\big([\tilde{\mathbf{p}}_u - \mathbf{p}_s]_2, [\tilde{\mathbf{p}}_u - \mathbf{p}_s]_1\big), \qquad (21a)$$

$$\tilde{\theta}_{s,u}^{\mathrm{el}} = \mathrm{asin}\Big(\frac{[(\tilde{\mathbf{p}}_u - \mathbf{p}_s)]_3}{\|\tilde{\mathbf{p}}_u - \mathbf{p}_s\|}\Big). \qquad (21b)$$

2) MCRB and LB Derivation: We denote the total temporal and spectral observation as $\mathbf{y}_{s,u} = [\mathbf{y}_{s,u}^{\mathsf{T}}[1, 1], \ldots, \mathbf{y}_{s,u}^{\mathsf{T}}[1, K], \ldots, \mathbf{y}_{s,u}^{\mathsf{T}}[L_{\mathrm{c}}, K]]^{\mathsf{T}} \in \mathbb{C}^{L_{\mathrm{c}}KN}$, where L_{c} represents the number of pilot symbols used for uplink channel estimation. Let $\boldsymbol{\eta}_{s,u} = [\Re(\vartheta_{s,u}), \Im(\vartheta_{s,u}), \tau_{s,u}]^{\mathsf{T}} \in \mathbb{R}^3$ collect the parameters to be estimated in the uplink channel estimation. The likelihood functions under the true and mismatched models are given by

$$\xi_{\mathrm{T}}(\mathbf{y}_{s,u}; \boldsymbol{\eta}_{s,u}) \propto e^{\|\mathbf{y}_{s,u} - \bar{\mathbf{g}}(\boldsymbol{\eta}_{s,u})\|^2} \qquad (22)$$

and

$$\xi_{\mathrm{M}}(\mathbf{y}_{s,u}; \boldsymbol{\eta}_{s,u}) \propto e^{\|\mathbf{y}_{s,u} - \tilde{\mathbf{g}}(\boldsymbol{\eta}_{s,u})\|^2}, \qquad (23)$$

respectively, where we define $\bar{\mathbf{g}}(\boldsymbol{\eta}_{s,u}) = [\bar{\mathbf{g}}_{s,u}^{\mathsf{T}}[1, 1], \ldots, \bar{\mathbf{g}}_{s,u}^{\mathsf{T}}[1, K], \ldots, \bar{\mathbf{g}}_{s,u}^{\mathsf{T}}[L_{\mathrm{c}}, K]]^{\mathsf{T}} \in \mathbb{C}^{L_{\mathrm{c}}KN}$ and $\tilde{\mathbf{g}}(\boldsymbol{\eta}_{s,u}) = [\tilde{\mathbf{g}}_{s,u}^{\mathsf{T}}[1, 1], \ldots, \tilde{\mathbf{g}}_{s,u}^{\mathsf{T}}[1, K], \ldots, \tilde{\mathbf{g}}_{s,u}^{\mathsf{T}}[L_{\mathrm{c}}, K]]^{\mathsf{T}} \in \mathbb{C}^{L_{\mathrm{c}}KN}$.

- *Pseudo-True Parameter:* According to Appendix A, the pseudo-true parameter, denoted by $\tilde{\boldsymbol{\eta}}_{s,u}$, is derived as

$$\tilde{\boldsymbol{\eta}}_{s,u} = \arg\min_{\boldsymbol{\eta}_{s,u}} \ \mathcal{D}\big\{\xi_{\mathrm{T}}(\mathbf{y}_{s,u}; \bar{\boldsymbol{\eta}}_{s,u}) \| \xi_{\mathrm{M}}(\mathbf{y}_{s,u}; \boldsymbol{\eta}_{s,u})\big\},$$

$$= \arg\min_{\boldsymbol{\eta}_{s,u}} \ \|\bar{\mathbf{g}}(\bar{\boldsymbol{\eta}}_{s,u}) - \tilde{\mathbf{g}}(\boldsymbol{\eta}_{s,u})\|^2, \qquad (24)$$

where the bar above the parameter emphasizes the ground-truth value. Once again, by employing gradient descent and treating truth parameter as initial point, the above problem can be efficiently solved [52].

- *MCRB:* The generalized FIMs, i.e., $\mathbf{A}_{\tilde{\boldsymbol{\eta}}_{s,u}}$ and $\mathbf{B}_{\tilde{\boldsymbol{\eta}}_{s,u}}$, are obtained by calculating the first- and second-order derivatives of $\tilde{\mathbf{q}}(\boldsymbol{\eta}_{s,u})$ with respect to the elements of $\boldsymbol{\eta}_{s,u}$, as described in Appendix C. Based on these, the MCRB is given by

$$\mathrm{MCRB}(\tilde{\boldsymbol{\eta}}_{s,u}) = \mathbf{A}_{\tilde{\boldsymbol{\eta}}_{s,u}}^{-1}\mathbf{B}_{\tilde{\boldsymbol{\eta}}_{s,u}}\mathbf{A}_{\tilde{\boldsymbol{\eta}}_{s,u}}^{-1}. \qquad (25)$$

- *LB:* The estimation error LB matrix is then calculated as

$$\mathrm{LBM}(\tilde{\boldsymbol{\eta}}_{s,u}) = \mathrm{MCRB}(\tilde{\boldsymbol{\eta}}_{s,u}) + \mathrm{Bias}(\tilde{\boldsymbol{\eta}}_{s,u}), \qquad (26)$$

[8]Note that although the TOA $\tau_{s,u}$ has already been estimated during the downlink positioning process, it will nevertheless be estimated during uplink channel estimation as part of standard OFDM processing [53]. This is necessary unless the UT and the LEO satellite are perfectly time-synchronized and the propagation delay remains precisely known, which are hardly satisfied in the highly dynamic LEO satellite environment.

where $\text{Bias}\left(\tilde{\boldsymbol{\eta}}_{s,u}\right) = \left(\bar{\boldsymbol{\eta}}_{s,u} - \tilde{\boldsymbol{\eta}}_{s,u}\right)\left(\bar{\boldsymbol{\eta}}_{s,u} - \tilde{\boldsymbol{\eta}}_{s,u}\right)^{\mathsf{T}}$. For an efficient estimator, the LB for the expected RMSE of the channel gain $\vartheta_{s,u}$ and the TOA $\tau_{s,u}$, in the presence of model mismatch, are expressed as

$$\text{LB}\left(\vartheta_{s,u}\right) = \sqrt{\text{Tr}\left(\left[\text{LBM}\left(\tilde{\boldsymbol{\eta}}_{s,u}\right)\right]_{1:2,1:2}\right)} \quad (27)$$

and

$$\text{LB}\left(\tau_{s,u}\right) = \sqrt{\left[\text{LBM}\left(\tilde{\boldsymbol{\eta}}_{s,u}\right)\right]_{3,3}}, \quad (28)$$

respectively.

IV. COOPERATIVE BEAMFORMING FOR DOWNLINK COMMUNICATIONS

The proposed two-timescale PACE enables channel reconstruction between each LEO satellite and all UTs, enabling CSI-based beamforming for downlink communication. To address the limited link budget in single-satellite downlink scenarios, we introduce multi-LEO satellite cooperative beamforming, where each UT is served by the satellites within the cluster simultaneously. Note that the cooperative beamforming optimization developed in this section is based on a *nominal* signal model, which treats the channel parameters estimated via PACE as true and assumes perfect delay/Doppler compensation across satellites. In contrast, the communication rate in the simulations is evaluated using the *ground-truth* channel parameters under imperfect compensation. *This separation enables a direct assessment of the effectiveness of PACE by examining the performance achieved by beamformers optimized with nominal (PACE-estimated) parameters. The smaller the performance gap between nominal- and ground-truth-optimized beamformers, the more reliable PACE can be considered.* Developing robust beamforming strategies that explicitly account for CSI uncertainty (e.g., [27], [54], [55]) and/or asynchronous interference due to imperfect compensation (e.g., [23]) represents an important but orthogonal research direction, which is left for future work.

A. Nominal Signal Model

In the nominal signal model, we assume perfect delay and Doppler compensation across all satellites. Under this assumption, the nominal channel, denoted by $\tilde{\mathbf{h}}_{s,u} = \tilde{\vartheta}_{s,u}\mathbf{a}(\tilde{\boldsymbol{\theta}}_{s,u})$, is frequency-flat, where the tilde denotes estimated values. This allows subcarrier-coherent beamforming, where the same beamformer is applied across all subcarriers, thereby reducing optimization complexity. Specifically, for the s-th LEO satellite transmitting over the k-th subcarrier, the signal is

$$\mathbf{x}_s\left[k\right] = \mathbf{W}_s\mathbf{s}\left[k\right], \quad (29)$$

where $\mathbf{W}_s = \left[\mathbf{w}_{s,1}, \mathbf{w}_{s,2}, \ldots, \mathbf{w}_{s,U}\right] \in \mathbb{C}^{N\times U}$ represents the beamformer for the s-th LEO satellite, and $\mathbf{s}\left[k\right] \sim \mathcal{CN}(\mathbf{0}, \mathbf{I}_U)$ denotes the data streams transmitted to the U UTs over the

---

Algorithm 1 Proposed Algorithm for Solving (32)

1: **Initialize**: $\mathbf{W}_s, \forall s$;
2: **repeat**
3:      Update μ_u using (34);
4:      Update ω_u using (35);
5:      **for** $s = 1 : S$ **do**
6:          Obtain eigenvalue decomposition of $\mathbf{R}_s$;
7:          Determine λ by Golden-section search over (53);
8:          Determine $\mathbf{w}_s$ via (54) and reshape to obtain $\mathbf{W}_s$;
9:      **end for**
10: **until** the reduction ratio of the objective value falls below a predefined threshold or a predetermined iteration number is reached;
11: **Output**: $\mathbf{W}_s, \forall s$.

---

k-th subcarrier. The received signal at the u-th UT over the k-th subcarrier is then

$$y_u\left[k\right] = \sum_{s=1}^{S}\tilde{\mathbf{h}}_{s,u}^{\mathsf{T}}\mathbf{w}_{s,u}s_u\left[k\right] + \underbrace{\sum_{m\neq u}^{U}\sum_{s=1}^{S}\tilde{\mathbf{h}}_{s,u}^{\mathsf{T}}\mathbf{w}_{s,m}s_m\left[k\right]}_{\text{Inter-user interference}} + z_u\left[k\right],$$

(30)

where $z_u[k] \sim \mathcal{CN}(0, N_0\Delta f)$ denotes the AWGN.

The nominal achievable communication rate for the u-th UT, aggregated across all subcarriers, is given by

$$\tilde{R}_u = B\log_2\left(1 + \frac{\left|\sum\limits_{s=1}^{S}\tilde{\mathbf{h}}_{s,u}^{\mathsf{T}}\mathbf{w}_{s,u}\right|^2}{\sum\limits_{m\neq u}^{U}\left|\sum\limits_{s=1}^{S}\tilde{\mathbf{h}}_{s,u}^{\mathsf{T}}\mathbf{w}_{s,m}\right|^2 + N_0\Delta f}\right). \quad (31)$$

B. Problem Formulation

We aim to optimize the beamformers at each LEO satellite to maximize the sum rate of all UTs. The optimization problem is formulated as follows

$$\max_{\mathbf{W}_s} \quad \sum_{u=1}^{U}\tilde{R}_u$$

$$\text{s.t.} \quad \sum_{u=1}^{U}\|\mathbf{w}_{s,u}\|^2 \leq \frac{P_s}{K}, \ \forall s, \quad (32)$$

where P_s denotes the power budget at the s-th LEO satellite.

C. Proposed Cooperative Beamforming Approach

In the following, we employ the WMMSE optimization framework [56] to solve (32) iteratively. Specifically, by introducing the auxiliary variables μ_u and ω_u, where μ_u and ω_u serve as the MMSE equalizer and weight, respectively [56], (32) can be equivalently reformulated as

$$\max_{\mu_u, \omega_u, \mathbf{W}_s} \quad \sum_{u=1}^{U}\left(\ln\omega_u - \omega_u\Psi_u\right)$$

$$\text{s.t.} \quad \sum_{u=1}^{U}\|\mathbf{w}_{s,u}\|^2 \leq \frac{P_s}{K}, \ \forall s, \quad (33)$$

where $\Psi_u = |1 - \mu_u \sum_{s=1}^{S} \tilde{\mathbf{h}}_{s,u}^{\mathsf{T}} \mathbf{w}_{s,u}|^2 + |\mu_u|^2 (\sum_{m\neq u}^{U} |\sum_{s=1}^{S} \tilde{\mathbf{h}}_{s,u}^{\mathsf{T}} \mathbf{w}_{s,m}|^2 + N_0 \Delta f)$. The optimization problem in (33) is solved by iteratively updating $\mathbf{W}_s$, ω_u, and μ_u, as detailed below.

1) Update μ_u: With ω_u and $\mathbf{W}_s$ fixed, the optimal μ_u is derived by setting $\partial \Psi_u / \partial \mu_u = 0$, resulting in

$$\mu_u = \frac{\left(\sum_{s=1}^{S} \tilde{\mathbf{h}}_{s,u}^{\mathsf{T}} \mathbf{w}_{s,u}\right)^*}{\sum_{m=1}^{U} \left|\sum_{s=1}^{S} \tilde{\mathbf{h}}_{s,u}^{\mathsf{T}} \mathbf{w}_{s,m}\right|^2 + N_0 \Delta f}. \tag{34}$$

2) Update ω_u: With μ_u and $\mathbf{W}_s$ fixed, the optimal ω_u is obtained by setting $\partial \Psi_u / \partial \omega_u = 0$, leading to

$$\omega_u = \frac{1}{\Psi_u}. \tag{35}$$

3) Update $\mathbf{W}_s$: With μ_u and ω_u fixed, the optimization problem to find the optimal $\mathbf{W}_s$ is formulated as

$$\min_{\mathbf{W}_s} \quad \sum_{u=1}^{U} \omega_u \Psi_u$$
$$\text{s.t.} \quad \sum_{u=1}^{U} \|\mathbf{w}_{s,u}\|^2 \leq \frac{P_s}{K}, \ \forall s. \tag{36}$$

Here, Ψ_u can be expressed as the sum of a positive semi-definite quadratic form and a linear term.

We note that (36) is a convex QCQP with respect to $\mathbf{W}_s$, which can be solved using standard toolboxes such as CVX. However, this approach incurs a per-iteration complexity of $\mathcal{O}((SNU)^3)$, since the beamformers of all satellites are optimized jointly. To better suit computation resource-constrained LEO scenarios, we instead develop a low-complexity method that strategically exploits BCD, strong duality, and matrix inversion properties.[9] This reduces the dominant complexity of solving (36) from $\mathcal{O}((SNU)^3)$ to $\mathcal{O}(SN^3)$. Further details are provided in Appendix D. The overall procedure for solving (32) is summarized in Algorithm 1, and its convergence follows directly from the BCD structure of the algorithm.

D. Evaluation Model

As stated above, after obtaining the cooperative beamformers by solving the optimization problem under the *nominal* signal model (with PACE-estimated channel parameters and

---

[9]Despite the significant complexity reduction enabled by the proposed scheme, we note that the optimization is still carried out in a centralized manner (e.g., at a cluster-head satellite), which may incur scalability bottlenecks as the network size grows. Designing decentralized strategies that distribute the optimization across participating satellites to improve scalability is an important research direction but lies beyond the scope of this paper. We refer interested readers to our recent work [57] for a scalable distributed beamforming framework over networked LEO satellites.

ideal inter-satellite compensation), we evaluate the achievable communication performance using a more realistic *evaluation* model that employs the *ground-truth* channel parameters and explicitly accounts for practical compensation imperfections. This separation is intentional: it enables a direct assessment of the effectiveness of PACE by examining how well beamformers optimized with nominal (PACE-estimated) parameters perform when deployed in a realistic setting.

Following the Doppler-compensation-free assumption adopted in [18], [24], we do not rely on explicit Doppler precompensation at the transmitter in the evaluation model for simplicity. Meanwhile, we account for imperfect delay compensation, which induces residual phase rotations across subcarriers. In addition, motivated by [22], [23], [58], we further incorporate the resulting *asynchronous interference* due to link-dependent delay mismatch across users in multi-LEO cooperative transmission.

Specifically, after delay precompensation, the received signal of u-th UT on k-th subcarrier is modeled as[10]

$$y_u[k] = \sum_{s=1}^{S} e^{-\jmath 2\pi k \Delta f (\tau_{s,u} - \tilde{\tau}_{s,u})} \bar{\mathbf{h}}_{s,u}^{\mathsf{T}}[k] \mathbf{w}_{s,u} \, s_u[k] \tag{37}$$
$$+ \sum_{m\neq u}^{U} \sum_{s=1}^{S} e^{-\jmath 2\pi k \Delta f (\tau_{s,u} - \tilde{\tau}_{s,m})} \bar{\mathbf{h}}_{s,u}^{\mathsf{T}}[k] \mathbf{w}_{s,m} \, s_m[k] + z_u[k],$$

where $\bar{\mathbf{h}}_{s,u}[k] = \alpha_{s,u} G(\theta_{s,u}^{\text{el}}) \mathbf{a}(\boldsymbol{\theta}_{s,u})$ denotes the (approximately) frequency-flat array response term, while the residual delay mismatch is explicitly captured by the subcarrier-dependent phase rotations in (37).

Accordingly, the achievable rate of u-th UT under the evaluation model is given by (38) at the bottom of this page, which makes explicit that asynchronous interference persists due to *link-dependent delay mismatch across users*, even after applying delay precompensation.

V. NUMERICAL RESULTS

A. Simulation Parameters

We model the Earth as a sphere with a radius of 6400 km and adopt a spherical coordinate system centered at the Earth's core. The UTs are randomly distributed in a circular service area on the Earth's surface with a radius of 200 km [28]. The participating LEO satellites are positioned within a corresponding circular area in space, centered along the extension of the line connecting the Earth's core to the center of the surface service area, at an orbital altitude of 500 km. Each satellite

---

[10]Note that we assume the difference between $\tilde{\tau}_{s,m}$ and $\tau_{s,m}$ is smaller than the cyclic prefix (CP) length.

$$R_u = \Delta f \sum_{k=1}^{K} \log_2 \left(1 + \frac{\left|\sum_{s=1}^{S} e^{-\jmath 2\pi k \Delta f (\tau_{s,u} - \tilde{\tau}_{s,u})} \bar{\mathbf{h}}_{s,u}^{\mathsf{T}}[k] \, \mathbf{w}_{s,u}\right|^2}{\sum_{m\neq u}^{U} \left|\sum_{s=1}^{S} e^{-\jmath 2\pi k \Delta f (\tau_{s,u} - \tilde{\tau}_{s,m})} \bar{\mathbf{h}}_{s,u}^{\mathsf{T}}[k] \, \mathbf{w}_{s,m}\right|^2 + N_0 \Delta f}\right), \tag{38}$$

Parameter	Value
Central carrier frequency f_c	12.7 GHz (Ku band)
Subcarrier spacing Δf	120 KHz
Subcarrier number K	1024
Power budget at each LEO satellite	50 dBm
Power budget at each UT	40 dBm
PSD N_0	-173.855 dBm/Hz
Noise figure F	10 dB
Number of LEO satellites S	4
Number of UTs U	8
Antenna number $N = N_{\mathrm{h}} \times N_{\mathrm{v}}$	16×16
Antenna radiation gain $G(\cdot)$	$\sqrt{\frac{3}{4\pi}}\cos(\theta)$ [39]

travels along an orbital path intersecting this line at a constant speed $|\mathbf{v}_s| = 7.6$ km/s, with velocity vectors $\mathbf{v}_s$ tangent to their orbits and UPAs oriented toward Earth's core. Due to imperfect time-domain and frequency-domain synchronization, the clock bias (respectively, CFO) between each satellite and the UT is randomly set to a value between 8 ns and 12 ns (respectively, between $\Delta f/120$ and $\Delta f/80$), which remains fixed throughout the simulation. To eliminate satellite handover involvement, we consider one large-timescale position-coherent frame containing 100 small-timescale channel gain-coherent subframes, where the channel gain changes independently from one subframe to another. Throughout this frame, the satellite constellation topology remains constant for simplicity. The downlink positioning and uplink channel estimation consist of $L_{\mathrm{p}} = 10000$ and $L_{\mathrm{c}} = 1000$ pilot symbols, respectively.

The channel gain from each LEO satellite to each UT, expressed by (3), is independently generated in each channel-gain coherent slot. The random phase $\psi_{s,u}$ is uniformly cooperative in $[0, 2\pi]$. The components that constitute the path loss $\beta_{s,u}$ are generated according to (4). The free-space path loss is given by $\beta_{s,u}^{\mathrm{FS}} = 20 \log_{10}(\|\mathbf{p}_u - \mathbf{p}_s\|) + 20 \log_{10}(f_c) - 147.55$ [dB] [41]. The atmospheric absorption $\beta_{s,u}^{\mathrm{AB}}$, which depends on signal frequency and satellite elevation angle, is calculated according to International Telecommunication Union (ITU) recommendations [59] and configured using an off-the-shelf MATLAB script [36]. In the considered LOS-dominant suburban/rural/remote scenarios, the clutter loss $\beta_{s,u}^{\mathrm{CL}}$ and the shadow fading $\beta_{s,u}^{\mathrm{SF}}$ originating from near-surface structures are typically weak [60]. Therefore, we set $\beta_{s,u}^{\mathrm{CL}} = 0$ dB and $\beta_{s,u}^{\mathrm{SF}} = 0$ dB for convenience. Additionally, ionospheric scintillation can be ignored for frequencies above 6 GHz [41]. For $\beta_{s,u}^{\mathrm{CL}}$ caused by tropospheric scintillation, which is generally difficult to model analytically, we adopt the example suggested in [36] as a reference value. The remaining simulation parameters are listed in Table I.

B. Compared Schemes

1) Downlink Positioning: Since we do not optimize the beamforming matrix $\mathbf{F}_s$, it is generated directly based on two principles, which differ depending on whether position information is utilized:

- Position-Aided Beamforming (PAB): Leveraging the position information of UTs obtained from the previous position-coherent frame, each LEO satellite constructs $\mathbf{F}_s$ as a matrix whose columns correspond to the conjugates of the steering vectors for the UTs' estimated directions. Specifically, $\mathbf{F}_s = \bar{\zeta}_s [\mathbf{a}^*(\hat{\boldsymbol{\theta}}_{s,1}), \ldots, \mathbf{a}^*(\hat{\boldsymbol{\theta}}_{s,U})]$, where $\bar{\zeta}_s$ is a normalization factor that ensures compliance with the power budget.
- Vertically Directed Beamforming (VDB): In the absence of position information, each LEO satellite generates a vertical beam directed toward the Earth's core. In this case, the beamforming matrix reduces to a steering vector with an elevation angle of $\pi/2$.

2) Uplink Channel Estimation: Depending on the availability of position information at the LEO satellites, we consider three types of schemes for evaluating the performance of uplink channel estimation:

- PACE: This is the proposed two-timescale hybrid downlink positioning and uplink channel estimation scheme. Its performance is rigorously characterized through MCRB analysis.
- Perfect-PACE: This represents an ideal benchmark where perfect position information of the UTs is assumed to be available at the LEO satellites. In this case, the performance of uplink channel estimation is evaluated without model mismatch and analyzed using the CRB.
- Uplink Channel Estimation (UCE): As previously discussed, in the absence of position information, the channel vector, i.e., $\mathbf{h}_{s,u}[k] = e^{-j2\pi k \Delta f \tau_{s,u}} \alpha_{s,u} G(\theta_{s,u}^{\mathrm{el}}) \mathbf{a}(\boldsymbol{\theta}_{s,u})$, can be directly estimated in the uplink using a *geometry-agnostic* approach. By defining $\mathbf{h}_{s,u} = \alpha_{s,u} G(\theta_{s,u}^{\mathrm{el}}) \mathbf{a}(\boldsymbol{\theta}_{s,u})$, we analyze the performance limits of estimating $\mathbf{h}_{s,u}$ and $\tau_{s,u}$ simultaneously by deriving the CRB. This derivation extends the approach in [53], which was originally developed for a single-carrier system.

3) Downlink Communication: To evaluate downlink communication performance, we use the estimated CSI from the channel estimation schemes above to perform cooperative beamforming, as outlined in Algorithm 1 (since the satellites only have access to estimated CSI). The resulting beamformer is then tested with ground-truth CSI to obtain the actual sum rate. We also consider two benchmark schemes:

- PAB: This approach is the same as the one introduced for downlink positioning.
- No-Cooperation (NC): In this method, each UT is served only by the single LEO satellite with the strongest signal strength, thereby avoiding inter-satellite cooperation. The WMMSE algorithm is applied independently at each satellite to optimize its beamformers based solely on its own CSI for the associated UTs, while signals from other satellites are treated as interference.

C. Downlink Positioning

As shown in Fig. 3, we compare the positioning error bounds and biases under PAB and VDB with different per-
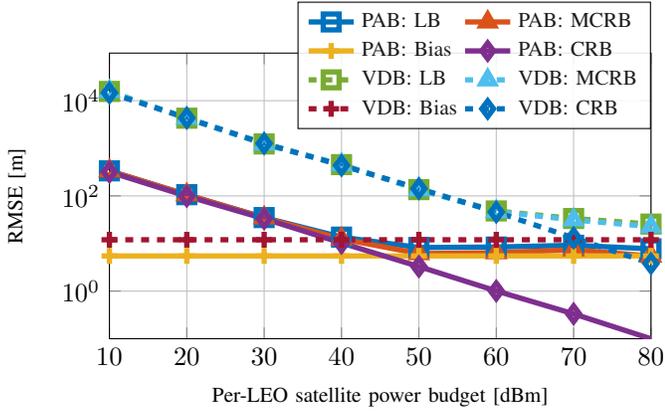
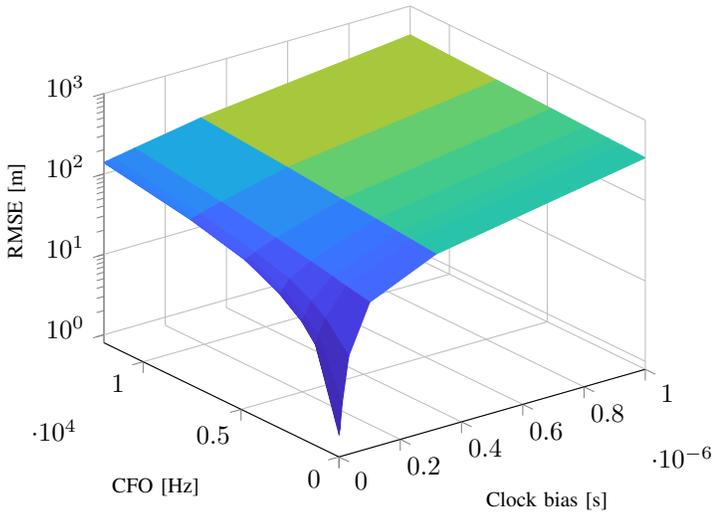Fig. 3. Positioning RMSE LB versus per-LEO satellite power budget.

Fig. 4. Positioning RMSE LB versus maximum clock bias and CFO.

satellite power budget. The results reveal that the LB of positioning error without model mismatch, represented by the positioning CRB under perfectly time- and frequency-synchronized satellites, decreases as the transmit power increases. In contrast, when synchronization mismatch is present, the LB initially decreases but eventually saturates due to the persistent positioning bias, which remains unaffected by the transmit power. This highlights the detrimental impact of imperfect time- and frequency-synchronization among LEO satellites on positioning performance [35], [37], potentially leading to overly optimistic performance evaluations. Furthermore, PAB consistently outperforms VDB by achieving a lower LB, with the performance gain being particularly significant (over an order of magnitude) at lower yet more practical transmit power levels. This advantage stems from PAB's ability to leverage position information to allocate more power to the UTs than VDB, underscoring the importance of incorporating prior position knowledge into the design of positioning systems.

In Fig. 4, we analyze the impact of varying clock bias and CFO among satellite–UT pairs on the LB of positioning

error (under PAB), where both impairments are assumed to be uniformly distributed between 0 and their respective maximum values. The results show that positioning performance degrades significantly as either factor increases. In particular, even a clock bias on the order of tens to hundreds of nanoseconds or a CFO of several kHz can lead to positioning errors exceeding 100 m. These findings highlight the comparable severity of both impairments and underscore the critical importance of *mitigating mismatches in both the time and frequency domains* to ensure high-accuracy LEO positioning.
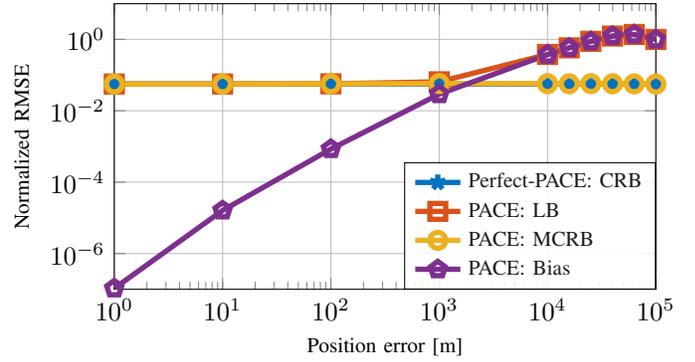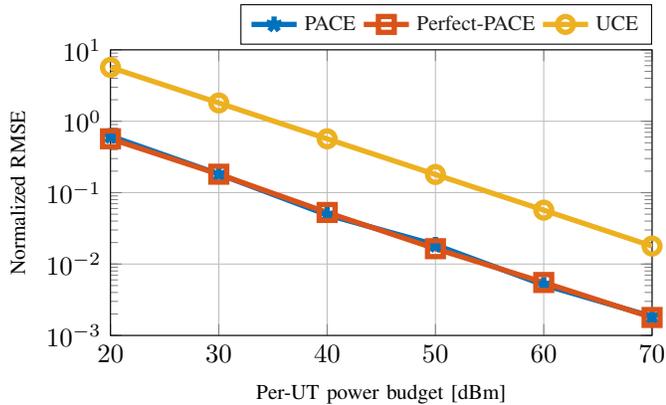

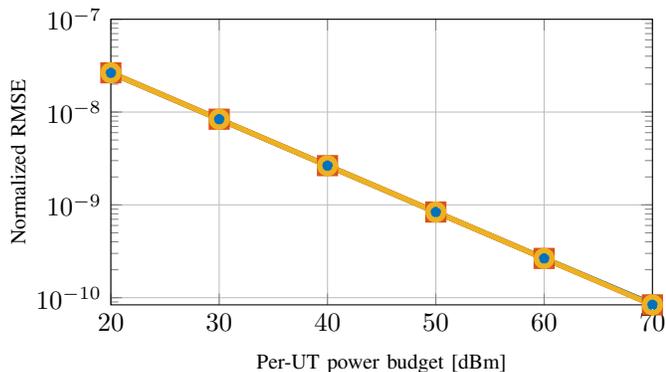(a) Channel gain estimation
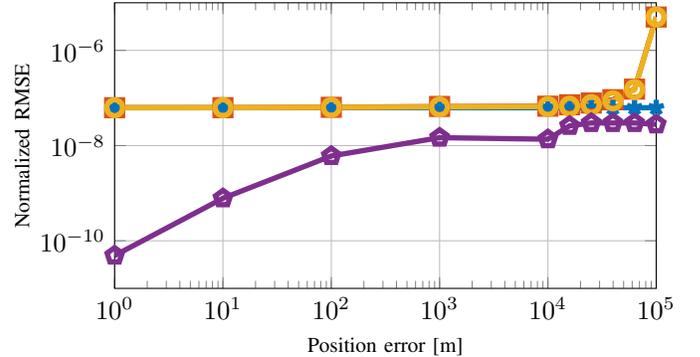
(b) TOA estimation

Fig. 5. Uplink channel estimation RMSE LB versus positioning error: (a) Channel vector estimation; (b) TOA estimation.

D. Uplink Channel Estimation

In Figs. 5(a) and (b), we evaluate the normalized RMSE, obtained by dividing the RMSE by the ground-truth parameters, for both channel gain and TOA estimation using our proposed PACE, under varying positioning errors. The results are compared with those of Perfect-PACE, which assumes no model mismatch due to positioning errors. The results reveal that when positioning errors are small, PACE's LB closely matches that of Perfect-PACE for both parameters. However, as positioning errors increase, PACE's performance deteriorates due to growing model mismatch. For channel gain estimation, we observe that while the MCRB-induced error remains relatively insensitive to positioning errors, the bias component increases proportionally with positioning error, eventually becoming the primary contributor to the overall channel gain error. The TOA estimation exhibits different behavior: its bias initially increases with positioning error

(a) Channel vector estimation

(b) TOA estimation

Fig. 6. Uplink channel estimation RMSE LB versus per-UT power budget: (a) Channel vector estimation; (b) TOA estimation.

before reaching a plateau, whereas the MCRB-induced error continues to grow, ultimately becoming the dominant factor in the total TOA estimation error. Nevertheless, the results indicate that channel estimation degrades noticeably only when the positioning error becomes *impractically large* (e.g., exceeding 1 km). This observation highlights the robustness of PACE to positioning imperfections in LOS-dominant scenarios with relatively high satellite altitudes.

In Figs. 6(a) and (b), we compare the LB for the RMSE of both channel vector and TOA estimation using the proposed PACE against those obtained under UCE, versus UT's power budget. Note that PACE estimates both the channel gain $\alpha_{s,u}$ and the TOA $\tau_{s,u}$, whereas UCE estimates the channel vector $\boldsymbol{h}_{s,u} = \alpha_{s,u}G(\theta_{s,u}^{\text{el}})\mathbf{a}(\boldsymbol{\theta}_{s,u})$ (excluding the TOA-induced phase) in addition to $\tau_{s,u}$. To enable a unified comparison, we transform the LB for channel gain estimation RMSE in PACE into the corresponding LB for channel vector estimation RMSE (using the form $\hat{\boldsymbol{h}}_{s,u} = \hat{\alpha}_{s,u}G(\hat{\theta}_{s,u}^{\text{el}})\mathbf{a}(\hat{\boldsymbol{\theta}}_{s,u})$) through algebraic manipulation. As shown, the TOA estimation performance of PACE closely aligns with that of UCE, given that negligible positioning error is incurred in the positioning stage. This alignment occurs because TOA estimation is independent of whether the other unknown parameter is the channel gain or the channel vector. This independence can be readily demonstrated by deriving the CRB for TOA estimation under Perfect-PACE and UCE, which we omit here due to space
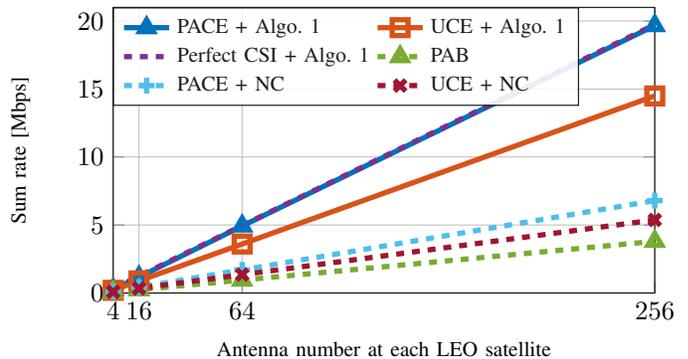

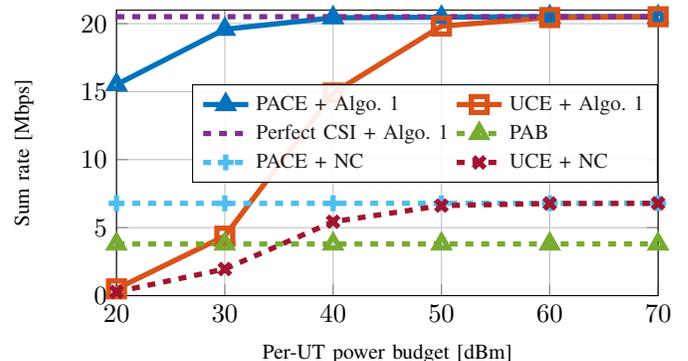Fig. 7. Sum rate versus per-LEO satellite antenna number.

Fig. 8. Sum rate versus per-UT power budget.

limitations. In contrast, PACE significantly outperforms UCE in channel vector estimation. This superiority is attributed to PACE's utilization of position information, which reduces the complexity of estimating a vector (as required by UCE) to that of estimating a scalar, albeit subject to positioning error. Consequently, PACE achieves higher channel estimation accuracy under the same pilot length and power budget.

E. Donwlink Communication

In Fig. 7, we compare the downlink communication sum rates achieved by various approaches as a function of the number of antennas deployed on each LEO satellite. It is observed that Algorithm 1 combined with PACE significantly outperforms UCE and other baseline methods, achieving sum rates that closely approach those obtained with perfect CSI. This superior performance is attributed to PACE's enhanced channel reconstruction accuracy and the benefits of multi-LEO satellite cooperation. In contrast, the sum rate under NC, whether using PACE or UCE, remains consistently higher than that achieved by PAB, even though PAB leverages inter-satellite cooperation. This highlights the critical role of accurate CSI in enhancing downlink communication efficiency, beyond what can be achieved using position information alone. Moreover, as the number of antennas per LEO satellite increases, the performance advantage of the proposed scheme, i.e., the combination of PACE and Algorithm 1, becomes increasingly pronounced, demonstrating its potential for enabling high-throughput LEO satellite communications with large-scale antenna arrays.

As shown in Fig. 8, we compare the sum rates under various schemes versus the per-UT power budget. It can be observed that the sum rate under PAB is independent of the UTs' transmit power. In contrast, as the UTs' transmit power increases, the sum rates achieved by Algorithm 1 and NC also increase. This is because higher transmit power improves channel estimation accuracy, which in turn reduces the mismatch between the channel parameters used to optimize beamforming and the ground-truth ones, thereby enhancing the resultant sum rate. Specifically, the sum rates achieved by Algorithm 1 significantly outperform those under NC and PAB, and gradually approach the performance achieved with perfect CSI. This demonstrates the superiority of multi-LEO satellite cooperative beamforming. Moreover, the use of PACE results in a substantially higher sum rate compared to UCE, especially when the UTs' transmit power is low, due to its superior channel estimation accuracy. This highlights the importance of leveraging position information to obtain accurate CSI when the power budget at the UTs is limited, an aspect particularly relevant for power-constrained devices such as cell phones.

VI. Conclusion

This paper presents a novel framework for integrating positioning and communication in multi-LEO satellite systems, leveraging positioning capabilities to enhance channel estimation and thereby facilitate communication. By capitalizing on the distinct timescale variations of position-related parameters and channel gains, we propose a two-timescale frame structure that strategically schedules downlink positioning, uplink channel estimation, and downlink communication. A rigorous MCRB-based analysis characterizes the impact of practical imperfections, including inter-satellite clock bias and CFO, on positioning accuracy. Additionally, we theoretically demonstrate through MCRB analysis how position information improves uplink channel estimation even under inevitable positioning errors. To overcome the limited link budget offered by single-satellite-based downlink communication, we introduce a multi-satellite cooperative beamforming optimization scheme to serve each UT simultaneously with multiple satellites within a cluster while reducing complexity. Numerical results validate our theoretical findings.

Beyond the positioning-aided communication emphasized in this work, studying the reverse direction is equally important for future research. For example, inter-UT sidelink communication and ranging enable information exchange among proximal UTs and provide independent timing and distance references. Such mechanisms are promising for mitigating inter-satellite clock biases and thereby improving overall positioning accuracy.

APPENDIX A
MCRB BASICS

This subsection briefly recaps the fundamentals of MCRB. For a parameter $\bar{\boldsymbol{\theta}} \in \mathbb{R}^{M \times 1}$, the LB matrix of the mean squared error of a mismatched estimator is provided by [38]

$$\text{LBM}(\tilde{\boldsymbol{\theta}}) = \underbrace{\mathbf{A}_{\tilde{\boldsymbol{\theta}}}^{-1} \mathbf{B}_{\tilde{\boldsymbol{\theta}}} \mathbf{A}_{\tilde{\boldsymbol{\theta}}}^{-1}}_{\text{MCRB}(\tilde{\boldsymbol{\theta}})} + \underbrace{\left(\bar{\boldsymbol{\theta}} - \tilde{\boldsymbol{\theta}}\right)\left(\bar{\boldsymbol{\theta}} - \tilde{\boldsymbol{\theta}}\right)^{\top}}_{\text{Bias}(\tilde{\boldsymbol{\theta}})}. \quad (39)$$

Here, $\tilde{\boldsymbol{\theta}}$ denotes the pseudo-true parameter obtained by

$$\tilde{\boldsymbol{\theta}} = \arg\min_{\boldsymbol{\theta}} \mathcal{D}\left\{\xi_{\text{T}}\left(\mathbf{y}; \bar{\boldsymbol{\theta}}\right) \| \xi_{\text{M}}\left(\mathbf{y}; \boldsymbol{\theta}\right)\right\}, \quad (40)$$

where $\mathcal{D}\{\xi_{\text{T}}\left(\mathbf{y}; \boldsymbol{\theta}\right) \| \xi_{\text{M}}(\mathbf{y}; \tilde{\boldsymbol{\theta}})\}$ denotes the Kullback-Leibler (KL) divergence between the true likelihood function $\xi_{\text{T}}\left(\mathbf{y}; \boldsymbol{\theta}\right)$ and the mismatched likelihood function $\xi_{\text{M}}(\mathbf{y}; \tilde{\boldsymbol{\theta}})$. In addition, $\mathbf{A}_{\tilde{\boldsymbol{\theta}}}$ and $\mathbf{B}_{\tilde{\boldsymbol{\theta}}}$ represent two generalized FIMs, whose elements in the i-th row and the j-th column are determined by [38]

$$\left[\mathbf{A}_{\tilde{\boldsymbol{\theta}}}\right]_{i,j} = \mathbb{E}_{f_T}\left\{\frac{\partial^2 \ln \xi_M\left(\mathbf{y}; \boldsymbol{\theta}\right)}{\partial\left[\boldsymbol{\theta}\right]_i \partial\left[\boldsymbol{\theta}\right]_j}\bigg|_{\boldsymbol{\theta}=\tilde{\boldsymbol{\theta}}}\right\}$$

$$= 2\Re\left\{\left(\frac{\partial^2 \boldsymbol{\mu}\left(\boldsymbol{\theta}\right)}{\partial\left[\boldsymbol{\theta}\right]_i \partial\left[\boldsymbol{\theta}\right]_j}\right)^{\mathsf{H}} \mathbf{C}_{\text{M}}^{-1} \boldsymbol{\epsilon}\left(\boldsymbol{\theta}\right)\right. \quad (41)$$

$$\left. - \left(\frac{\partial \boldsymbol{\mu}\left(\boldsymbol{\theta}\right)}{\partial\left[\boldsymbol{\theta}\right]_i}\right)^{\mathsf{H}} \mathbf{C}_{\text{M}}^{-1} \left(\frac{\partial \boldsymbol{\mu}\left(\boldsymbol{\theta}\right)}{\partial\left[\boldsymbol{\theta}\right]_j}\right)\right\}\bigg|_{\boldsymbol{\theta}=\tilde{\boldsymbol{\theta}}},$$

and

$$\left[\mathbf{B}_{\tilde{\boldsymbol{\theta}}}\right]_{i,j} = \mathbb{E}_{f_T}\left\{\frac{\partial \ln f_M\left(\mathbf{y}; \boldsymbol{\theta}\right)}{\partial\left[\boldsymbol{\theta}\right]_i}\bigg|_{\boldsymbol{\theta}=\tilde{\boldsymbol{\theta}}} \frac{\partial \ln f_M\left(\mathbf{y}; \boldsymbol{\theta}\right)}{\partial\left[\boldsymbol{\theta}\right]_j}\bigg|_{\boldsymbol{\theta}=\tilde{\boldsymbol{\theta}}}\right\}$$

$$= 4\Re\left\{\boldsymbol{\epsilon}\left(\boldsymbol{\theta}\right)^{\mathsf{H}} \mathbf{C}_{\text{M}}^{-1} \frac{\partial \boldsymbol{\mu}\left(\boldsymbol{\theta}\right)}{\partial\left[\boldsymbol{\theta}\right]_i}\right\} \Re\left\{\boldsymbol{\epsilon}\left(\boldsymbol{\theta}\right)^{\mathsf{H}} \mathbf{C}_{\text{M}}^{-1} \frac{\partial \boldsymbol{\mu}\left(\boldsymbol{\theta}\right)}{\partial\left[\boldsymbol{\theta}\right]_j}\right\}$$

$$+ 2\Re\left\{\left(\frac{\partial \boldsymbol{\mu}\left(\boldsymbol{\theta}\right)}{\partial\left[\boldsymbol{\theta}\right]_i}\right)^{\mathsf{H}} \mathbf{C}_{\text{M}}^{-1} \left(\frac{\partial \boldsymbol{\mu}\left(\boldsymbol{\theta}\right)}{\partial\left[\boldsymbol{\theta}\right]_j}\right)\right\}\bigg|_{\boldsymbol{\theta}=\tilde{\boldsymbol{\theta}}}, \quad (42)$$

respectively. Here, $\mathbf{C}_{\text{M}}$ represents the covariance matrix of $\xi_{\text{M}}(\mathbf{y}; \boldsymbol{\theta})$ and $\boldsymbol{\epsilon}(\tilde{\boldsymbol{\theta}}) = \boldsymbol{\kappa}(\bar{\boldsymbol{\theta}}) - \boldsymbol{\mu}(\tilde{\boldsymbol{\theta}})$ with $\boldsymbol{\kappa}(\bar{\boldsymbol{\theta}})$ and $\boldsymbol{\mu}(\tilde{\boldsymbol{\theta}})$ being the noise-free observations under the true and mismatched models, respectively [38], [52].

APPENDIX B
DERIVATIVES OF $\tilde{\mathbf{f}}\left(\mathbf{r}_u\right)$ WITH RESPECT TO $\mathbf{r}_u$

1) Non-Zero First-Order Derivative:

$$\frac{\partial \upsilon_{s,u}}{\partial \mathbf{p}_u} = \frac{\mathbf{v}_s}{\lambda \|\mathbf{p}_u - \mathbf{p}_s\|} - \frac{\left(\mathbf{v}_s^{\mathsf{T}}\left(\mathbf{p}_u - \mathbf{p}_s\right)\right)\left(\mathbf{p}_u - \mathbf{p}_s\right)}{\lambda \|\mathbf{p}_u - \mathbf{p}_s\|^3},$$

$$\frac{\partial \tau_{s,u}}{\partial \mathbf{p}_u} = \frac{\mathbf{p}_u - \mathbf{p}_s}{c \|\mathbf{p}_u - \mathbf{p}_s\|}, \quad \frac{\partial \upsilon_{s,u}}{\partial \delta_u} = 1, \quad \frac{\partial \tau_{s,u}}{\partial b_u} = 1.$$

2) Non-Zero Second-Order Derivative:

$$\frac{\partial^2 \upsilon_{s,u}}{\partial \mathbf{p}_u^2} = -\frac{\mathbf{v}_s\left(\mathbf{p}_u - \mathbf{p}_s\right)^{\mathsf{T}}}{\lambda \|\mathbf{p}_u - \mathbf{p}_s\|^3}$$

$$- \frac{\mathbf{v}_s\left(\mathbf{p}_u - \mathbf{p}_s\right)^{\mathsf{T}} + \mathbf{v}_s^{\mathsf{T}}\left(\mathbf{p}_u - \mathbf{p}_s\right)\mathbf{I}_3}{\lambda \|\mathbf{p}_u - \mathbf{p}_s\|^3}$$

$$+ \frac{3\left(\mathbf{v}_s^{\mathsf{T}}\left(\mathbf{p}_u - \mathbf{p}_s\right)\right)\left(\mathbf{p}_u - \mathbf{p}_s\right)\left(\mathbf{p}_u - \mathbf{p}_s\right)^{\mathsf{T}}}{\lambda \|\mathbf{p}_u - \mathbf{p}_s\|^5},$$

$$\frac{\partial^2 \tau_{s,u}}{\partial \mathbf{p}_u^2} = \frac{\mathbf{I}_3}{c \|\mathbf{p}_u - \mathbf{p}_s\|} - \frac{\left(\mathbf{p}_u - \mathbf{p}_s\right)\left(\mathbf{p}_u - \mathbf{p}_s\right)^{\mathsf{T}}}{c \|\mathbf{p}_u - \mathbf{p}_s\|^3}.$$

Note that the derivatives $\partial\tilde{\mathbf{g}}(\boldsymbol{\eta}_{s,u})/\partial[\boldsymbol{\eta}_{s,u}]_i$ and $\partial^2\tilde{\mathbf{g}}(\boldsymbol{\eta}_{s,u})/(\partial[\boldsymbol{\eta}_{s,u}]_i\partial[\boldsymbol{\eta}_{s,u}]_j)$ can be constructed by concatenating $\partial\tilde{\mathbf{g}}_{s,u}[\ell,k]/\partial[\boldsymbol{\eta}_{s,u}]_i$ and $\partial^2\tilde{\mathbf{g}}_{s,u}[\ell,k]/(\partial[\boldsymbol{\eta}_{s,u}]_i\partial[\boldsymbol{\eta}_{s,u}]_j)$, respectively, for $\ell = 1, \ldots, L_c$ and $k = 1, \ldots, K$. For simplicity, we provide the latter below.

1) Non-Zero First-Order Derivative:

$$\frac{\partial\tilde{\mathbf{g}}_{s,u}[\ell,k]}{\partial\Re\{\vartheta s,u\}} = e^{-j2\pi k\Delta f\tau_{s,u}}\tilde{\mathbf{d}}_{s,u}[\ell,k],$$

$$\frac{\partial\tilde{\mathbf{g}}_{s,u}[\ell,k]}{\partial\Im\{\vartheta_{s,u}\}} = je^{-j2\pi k\Delta f\tau_{s,u}}\tilde{\mathbf{d}}_{s,u}[\ell,k],$$

$$\frac{\partial\tilde{\mathbf{g}}_{s,u}[\ell,k]}{\partial\tau_{s,u}} = -\vartheta_{s,u}j2\pi k\Delta fe^{-j2\pi k\Delta f\tau_{s,u}}\tilde{\mathbf{d}}_{s,u}[\ell,k].$$

2) Non-Zero Second-Order Derivative:

$$\frac{\partial^2\tilde{\mathbf{g}}_{s,u}[\ell,k]}{\partial\Re\{\vartheta_{s,u}\}\partial\tau_{s,u}} = -j2\pi k\Delta fe^{-j2\pi k\Delta f\tau_{s,u}}\tilde{\mathbf{d}}_{s,u}[\ell,k],$$

$$\frac{\partial^2\tilde{\mathbf{g}}_{s,u}[\ell,k]}{\partial\Im\{\vartheta_{s,u}\}\partial\tau_{s,u}} = 2\pi k\Delta fe^{-j2\pi k\Delta f\tau_{s,u}}\tilde{\mathbf{d}}_{s,u}[\ell,k],$$

$$\frac{\partial^2\tilde{\mathbf{g}}_{s,u}[\ell,k]}{\partial\tau_{s,u}^2} = -\vartheta_{s,u}(2\pi k\Delta f)^2e^{-j2\pi k\Delta f\tau_{s,u}}\tilde{\mathbf{d}}_{s,u}[\ell,k].$$

A. Extracting Per-Satellite Subproblem

To reduce complexity of solving (36), we instead adopt a BCD strategy, optimizing beamformers for each satellite sequentially while fixing the others. For the s-th satellite, the subproblem depends only on $\mathbf{w}_s = [\mathbf{w}_{s,1}^\mathsf{T}, \ldots, \mathbf{w}_{s,U}^\mathsf{T}]^\mathsf{T}$ and can be reformulated as

$$\min_{\mathbf{w}_s} \quad -2\sum_{u=1}^{U}\Re\left\{\omega_u\mu_u\mathbf{h}_{s,u}^\mathsf{T}\mathbf{w}_{s,u}\right\}$$

$$+\sum_{u=1}^{U}\sum_{m=1}^{U}\omega_u\left|\mu_u\right|^2\left|\mathbf{h}_{s,u}^\mathsf{T}\mathbf{w}_{s,m}+\Omega_{s,u,m}\right|^2$$

$$\text{s.t.} \quad \|\mathbf{w}_s\|^2 \leq \frac{P_s}{K}, \tag{47}$$

where $\Omega_{s,u,m} = \sum_{s'\neq s}^{S}\mathbf{h}_{s',u}^\mathsf{T}\mathbf{w}_{s',m}$.

Let $\mathbf{E}_u = [\mathbf{0}_{N\times N}, \ldots, \underbrace{\mathbf{I}_N}_{\text{The u-th matrix}}, \ldots, \mathbf{0}_{N\times N}] \in \mathbb{R}^{N\times NU}$ be the selection matrix. Through algebraic manipulation, the above can be recast as a convex QCQP

$$\min_{\mathbf{w}_s} \quad \mathbf{w}_s^\mathsf{H}\mathbf{Q}_s\mathbf{w}_s - 2\Re\left\{\mathbf{b}_s^\mathsf{H}\mathbf{w}_s\right\}$$

$$\text{s.t.} \quad \|\mathbf{w}_s\|^2 \leq \frac{P_s}{K}, \tag{48}$$

where

$$\mathbf{R}_s = \sum_{u=1}^{U}\omega_u\left|\mu_u\right|^2\mathbf{h}_{s,u}^*\mathbf{h}_{s,u}^\mathsf{T} \succeq \mathbf{0}_{N\times N}, \tag{49a}$$

$$\mathbf{Q}_s = \mathbf{I}_U \otimes \mathbf{R}_s, \tag{49b}$$

$$\mathbf{b}_s = \sum_{u=1}^{U}\omega_u\mu_u^*\mathbf{E}_u^\mathsf{T}\mathbf{h}_{s,u}^* - \sum_{u=1}^{U}\sum_{m=1}^{U}\omega_u\left|\mu_u\right|^2\Omega_{s,u,m}\mathbf{E}_m^\mathsf{T}\mathbf{h}_{s,u}^*.$$

B. Exploiting Strong Duality

It is straightforward to observe that the above problem is a convex QCQP involving only $\mathbf{w}_s$. Rather than relying on a convex solver such as CVX, which uses interior-point methods and incurs a complexity of $\mathcal{O}((NU)^3)$, we exploit the problem's strong duality to further reduce computational complexity. Specifically, the Lagrangian of the problem is

$$\mathcal{L}\left(\mathbf{w}_s, \lambda\right) = \mathbf{w}_s^\mathsf{H}\mathbf{Q}_s\mathbf{w}_s - 2\Re\left\{\mathbf{b}_s^\mathsf{H}\mathbf{w}_s\right\} - \lambda\left(\|\mathbf{w}_s\|^2 - \frac{P_s}{K}\right),$$

where $\lambda \geq 0$ is the Lagrangian multiplier associated with the power constraint. Then, the optimal solutions of (48) can be derived through examining its Karush–Kuhn–Tucker (KKT) conditions as follows

$$\left(\mathbf{Q}_s + \lambda\mathbf{I}_{NU}\right)\mathbf{w}_s = \mathbf{b}_s, \tag{50a}$$

$$\|\mathbf{w}_s\| = \sqrt{\frac{P_s}{K}}, \tag{50b}$$

$$\lambda \geq 0. \tag{50c}$$

It follows from (50a) that

$$\mathbf{w}_s = \left(\mathbf{Q}_s + \lambda\mathbf{I}_{NU}\right)^{-1}\mathbf{b}_s. \tag{51}$$

Therefore, we must choose λ such that $\|(\mathbf{Q}_s + \lambda\mathbf{I}_{NU})^{-1}\mathbf{b}_s\| = \sqrt{P_s/K}$. Define

$$g\left(\lambda\right) = \left\|(\mathbf{Q}_s + \lambda\mathbf{I}_{NU})^{-1}\mathbf{b}_s\right\|^2 - \frac{P_s}{K}. \tag{52}$$

Since $\|(\mathbf{Q}_s + \lambda_2\mathbf{I}_{NU})^{-1}\mathbf{b}_s\| = \sqrt{\mathbf{b}_s^\mathsf{H}(\mathbf{Q}_s + \lambda_2\mathbf{I}_{NU})^{-2}\mathbf{b}_s} < \sqrt{\mathbf{b}_s^\mathsf{H}(\mathbf{Q}_s + \lambda_1\mathbf{I}_{NU})^{-2}\mathbf{b}_s} = \|(\mathbf{Q}_s + \lambda_1\mathbf{I}_{NU})^{-1}\mathbf{b}_s\|$ for $\lambda_2 > \lambda_1 \geq 0$, it follows that $g(\lambda)$ is monotonically decreasing with respect to λ whenever $\mathbf{Q}_s \succeq \mathbf{0}_{NU}$, which always holds by examining (49a) and (49b). Based on this property, a unique λ can be efficiently identified using a simple line search method such as the Golden-section search.

C. Reducing Matrix Inversion Complexity

We note that (52) involves a NU-dimensional matrix inversion, which still incurs a computational complexity of $\mathcal{O}((NU)^3)$ per iteration of the line search. To reduce this complexity, we exploit the structure $\mathbf{Q}_s = \mathbf{I}_U \otimes \mathbf{R}_s$. Let $\mathbf{b}_s = [\mathbf{b}_{s,1}^\mathsf{T}, \ldots, \mathbf{b}_{s,U}^\mathsf{T}]^\mathsf{T}$, where $\mathbf{b}_{s,u} \in \mathbb{C}^N$. We then have

$$g\left(\lambda\right) = \left\|\left(\mathbf{I}_U \otimes \mathbf{R}_s + \lambda\mathbf{I}_{NU}\right)^{-1}\mathbf{b}_s\right\|^2 - \frac{P_s}{K}$$

$$= \left\|\left(\mathbf{I}_U \otimes (\mathbf{R}_s + \lambda\mathbf{I}_N)\right)^{-1}\mathbf{b}_s\right\|^2 - \frac{P_s}{K}$$

$$= \left\|\left(\mathbf{I}_U \otimes (\mathbf{R}_s + \lambda\mathbf{I}_N)^{-1}\right)\mathbf{b}_s\right\|^2 - \frac{P_s}{K}$$

$$= \left\|\left(\mathbf{I}_U \otimes \left(\mathbf{U}(\boldsymbol{\Lambda} + \lambda\mathbf{I}_N)^{-1}\mathbf{U}^\mathsf{H}\right)\right)\mathbf{b}_s\right\|^2 - \frac{P_s}{K}$$

$$= \sum_{u=1}^{U}\left\|\mathbf{U}(\boldsymbol{\Lambda} + \lambda\mathbf{I}_N)^{-1}\mathbf{U}^\mathsf{H}\mathbf{b}_{s,u}\right\|^2 - \frac{P_s}{K}$$

$$= \sum_{u=1}^{U}\sum_{n=1}^{N}\frac{\left|\varpi_{s,u,n}\right|^2}{\left(\lambda_n + \lambda\right)^2} - \frac{P_s}{K}, \tag{53}$$

where $\boldsymbol{\varpi}_{s,u} = [\varpi_{s,u,1}, \ldots, \varpi_{s,u,N}]^\mathsf{T} = \mathbf{U}^\mathsf{H}\mathbf{b}_{s,u}$. Here, $\mathbf{R}_s$ is decomposed as $\mathbf{R}_s = \mathbf{U}\boldsymbol{\Lambda}\mathbf{U}^\mathsf{H}$ via eigenvalue decompo-
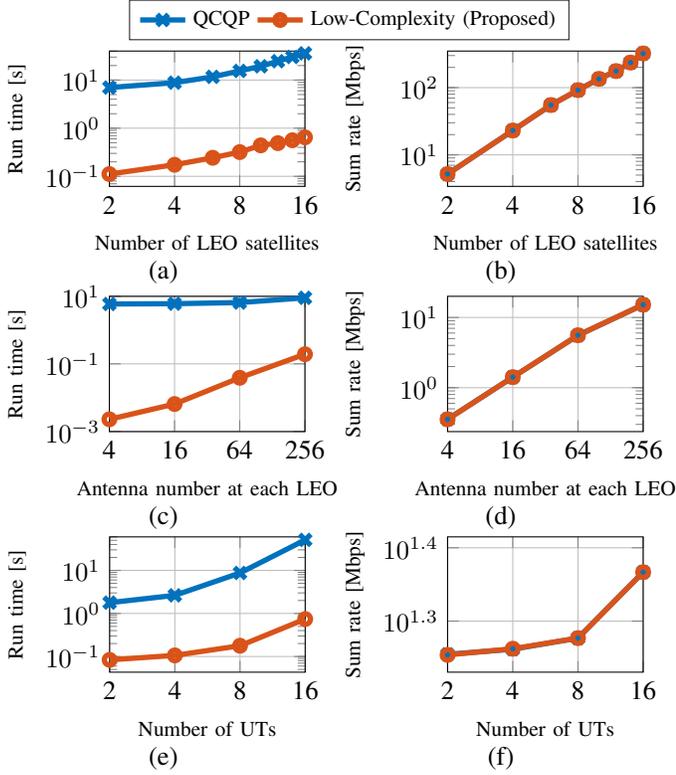
Fig. 9. Run time and sum rate comparison between the QCQP-based and proposed low-complexity algorithms: (a) Run time versus LEO satellite number; (b) Sum rate versus LEO satellite number; (c) Run time versus antenna number; (d) Sum rate versus antenna number; (e) Run time versus UT number; (f) Sum rate versus UT number.

sition, where $\mathbf{U} \in \mathbb{C}^{N \times N}$ is a unitary matrix and $\boldsymbol{\Lambda} = \mathrm{diag}[\lambda_1, \ldots, \lambda_N]$ is the diagonal eigenvalue matrix. Then, (51) is reformulated as

$$\mathbf{w}_s = \left(\mathbf{I}_U \otimes \left(\mathbf{U} \left(\boldsymbol{\Lambda} + \lambda \mathbf{I}_N \right)^{-1} \mathbf{U}^{\mathsf{H}} \right) \right) \mathbf{b}_s, \qquad (54)$$

which eliminates the need for an NU-dimensional matrix inversion and thereby reduces the computational complexity of updating beamformers.

D. Analyzing Complexity

The above reformulation shows that eigenvalue decomposition of the matrix $\mathbf{R}_s$ needs to be performed only once with complexity $\mathcal{O}(N^3)$, rather than repeatedly inverting an NU-dimensional matrix for each λ. The Golden-section search method, which has a linear convergence rate, finds an ϵ-solution within $\mathcal{O}(\log(1/\epsilon))$ iterations. Since each iteration only requires evaluating a one-dimensional function, the associated complexity can generally be neglected. Consequently, the eigenvalue decomposition step dominates the overall complexity of solving (47). As (47) is solved sequentially for $s = 1, \ldots, S$, the total complexity of solving (36) is reduced to $\mathcal{O}(SN^3)$, compared with the original $\mathcal{O}((SNU)^3)$.

To further demonstrate the superiority of the proposed algorithm, Fig. 9 compares the run time and sum rate of the QCQP-based and proposed low-complexity algorithms under varying numbers of LEO satellites, antennas per LEO, and UTs. The results show that the proposed algorithm, which

decomposes the beamformer update subproblem via BCD and exploits duality and line search, achieves orders-of-magnitude complexity reduction while maintaining identical sum-rate performance compared with the original QCQP-based update. This is notable since the QCQP formulation yields the optimal subproblem solution, whereas the proposed BCD-based structure converges only to a stationary point. These results validate the efficiency of the proposed low-complexity design.

REFERENCES

[1] Y. Zhang *et al.*, "Challenges and opportunities of future rural wireless communications," *IEEE Communications Magazine*, vol. 59, no. 12, pp. 16–22, 2021.

[2] J. G. Andrews *et al.*, "6G takes shape," *IEEE BITS the Information Theory Magazine*, pp. 1–38, 2024.

[3] G. Pan *et al.*, "Latency versus reliability in LEO mega-constellations: Terrestrial, aerial, or space relay?" *IEEE Transactions on Mobile Computing*, vol. 22, no. 9, pp. 5330–5345, 2023.

[4] J. An *et al.*, "Electromagnetic situation awareness and modeling for space–air–ground integrated networks," *National Science Review*, vol. 13, no. 1, p. nwaf492, 11 2025.

[5] T. Li *et al.*, "Ergodic capacity analysis for terrestrial-LEO-GEO relay systems with stochastic orbit modeling," *IEEE Transactions on Vehicular Technology*, vol. 74, no. 12, pp. 19 737–19 742, 2025.

[6] Y. Li *et al.*, "A signal reacquisition based on cross-entropy and postdetection with data modulation for LEO satellite communications," *IEEE Transactions on Aerospace and Electronic Systems*, vol. 61, no. 6, pp. 18 067–18 080, 2025.

[7] Z. Ni *et al.*, "LLM aided spectrum-sharing LEO satellite communications," *IEEE Journal on Selected Areas in Communications*, pp. 1–1, 2025.

[8] A. Papathanassiou *et al.*, "A comparison study of the uplink performance of W-CDMA and OFDM for mobile multimedia communications via LEO satellites," *IEEE Personal Communications*, vol. 8, no. 3, pp. 35–43, 2001.

[9] S. Liu *et al.*, "LEO satellite constellations for 5G and beyond: How will they reshape vertical domains?" *IEEE Communications Magazine*, vol. 59, no. 7, pp. 30–36, 2021.

[10] J. Ma *et al.*, "Integrated positioning and communication via LEO satellites: Opportunities and challenges," *arXiv preprint arXiv: 2411.14360*, 2024.

[11] K.-X. Li *et al.*, "Channel estimation for LEO satellite massive MIMO OFDM communications," *IEEE Transactions on Wireless Communications*, vol. 22, no. 11, pp. 7537–7550, 2023.

[12] M. Khammassi *et al.*, "Precoding for high-throughput satellite communication systems: A survey," *IEEE Communications Surveys & Tutorials*, vol. 26, no. 1, pp. 80–118, 2024.

[13] A. M. Darya *et al.*, "Semi-blind channel estimation for massive MIMO LEO satellite communications," *IEEE Communications Letters*, vol. 29, no. 1, pp. 75–79, 2025.

[14] P.-D. Arapoglou *et al.*, "MIMO over satellite: A review," *IEEE Communications Surveys & Tutorials*, vol. 13, no. 1, pp. 27–51, 2011.

[15] M. Y. Abdelsadek *et al.*, "Distributed massive MIMO for LEO satellite networks," *IEEE Open Journal of the Communications Society*, vol. 3, pp. 2162–2177, 2022.

[16] ——, "Broadband connectivity for handheld devices via LEO satellites: Is distributed massive MIMO the answer?" *IEEE Open Journal of the Communications Society*, vol. 4, pp. 713–726, 2023.

[17] Z. Xiang *et al.*, "Massive MIMO downlink transmission for multiple LEO satellite communication," *IEEE Transactions on Communications*, vol. 72, no. 6, pp. 3352–3364, 2024.

[18] Y.-Y. He *et al.*, "Physical beam sharing for communications with multiple low earth orbit satellites," *IEEE Transactions on Signal Processing*, vol. 72, pp. 2783–2798, 2024.

[19] X. Zhang *et al.*, "Multi-satellite cooperative networks: Joint hybrid beamforming and user scheduling design," *IEEE Transactions on Wireless Communications*, vol. 23, no. 7, pp. 7938–7952, 2024.

[20] D. Kim *et al.*, "Coverage analysis of dynamic coordinated beamforming for LEO satellite downlink networks," *IEEE Transactions on Wireless Communications*, vol. 23, no. 9, pp. 12 239–12 255, 2024.

[21] Y. Zhang *et al.*, "Distributed integrated sensing, localization, and communications over LEO satellite constellations," *IEEE Wireless Communications*, pp. 1–1, 2026.

[22] X. Chen *et al.*, "Asynchronous interference mitigation for LEO multi-satellite cooperative systems," *IEEE Transactions on Wireless Communications*, vol. 23, no. 10, pp. 14 956–14 971, 2024.

[23] S. Wu *et al.*, "Distributed beamforming for multiple LEO satellites with imperfect delay and doppler compensations: Modeling and rate analysis," *IEEE Transactions on Vehicular Technology*, vol. 74, no. 9, pp. 14 978–14 984, 2025.

[24] S. Kim *et al.*, "Cell-free massive non-terrestrial networks," *IEEE Journal on Selected Areas in Communications*, vol. 43, no. 1, pp. 201–217, 2025.

[25] R. Di Taranto *et al.*, "Location-aware communications for 5G networks: How location information can improve scalability, latency, and robustness of 5G," *IEEE Signal Processing Magazine*, vol. 31, no. 6, pp. 102–112, 2014.

[26] N. Gonzalez-Prelcic *et al.*, "Millimeter-wave communication with out-of-band information," *IEEE Communications Magazine*, vol. 55, no. 12, pp. 140–146, 2017.

[27] F. Jiang *et al.*, "Two-timescale transmission design and RIS optimization for integrated localization and communications," *IEEE Transactions on Wireless Communications*, vol. 22, no. 12, pp. 8587–8602, 2023.

[28] G. Kwon *et al.*, "Integrated localization and communication for efficient millimeter wave networks," *IEEE Journal on Selected Areas in Communications*, vol. 41, no. 12, pp. 3925–3941, 2023.

[29] G. Zhou *et al.*, "Individual channel estimation for RIS-aided communication systems—a general framework," *IEEE Transactions on Wireless Communications*, vol. 23, no. 9, pp. 12 038–12 053, 2024.

[30] Z. M. Kassas *et al.*, "Ad astra: Simultaneous tracking and navigation with megaconstellation LEO satellites," *IEEE Aerospace and Electronic Systems Magazine*, vol. 39, no. 9, pp. 46–71, 2024.

[31] R. M. Ferre *et al.*, "Is LEO-based positioning with mega-constellations the answer for future equal access localization?" *IEEE Communications Magazine*, vol. 60, no. 6, pp. 40–46, 2022.

[32] P. Zheng *et al.*, "LEO satellite and RIS: Two keys to seamless indoor and outdoor localization," *arXiv preprint arXiv:2312.16946*, 2025.

[33] H. K. Dureppagari *et al.*, "NTN-based 6G localization: Vision, role of LEOs, and open problems," *IEEE Wireless Communications*, vol. 30, no. 6, pp. 44–51, 2023.

[34] D.-R. Emenonye *et al.*, "Fundamentals of LEO-based localization," *IEEE Transactions on Information Theory*, vol. 71, no. 7, pp. 5277–5311, 2025.

[35] H. Xv *et al.*, "Joint beam scheduling and beamforming design for cooperative positioning in multi-beam LEO satellite networks," *IEEE Transactions on Vehicular Technology*, vol. 73, no. 4, pp. 5276–5287, 2024.

[36] P. Zheng *et al.*, "LEO- and RIS-empowered user tracking: A riemannian manifold approach," *IEEE Journal on Selected Areas in Communications*, vol. 42, no. 12, pp. 3445–3461, 2024.

[37] L. You *et al.*, "Integrated communications and localization for massive MIMO LEO satellite systems," *IEEE Transactions on Wireless Communications*, vol. 23, no. 9, pp. 11 061–11 075, 2024.

[38] S. Fortunati *et al.*, "Performance bounds for parameter estimation under misspecified models: Fundamental findings and applications," *IEEE Signal Processing Magazine*, vol. 34, no. 6, pp. 142–157, Nov. 2017.

[39] C. A. Balanis, *Antenna Theory: Analysis and Design*. Wiley-Interscience, 2005.

[40] H. Wymeersch *et al.*, "Radio localization and sensing—part I: Fundamentals," *IEEE Communications Letters*, vol. 26, no. 12, pp. 2816–2820, 2022.

[41] 3GPP, "Study on New Radio (NR) to support non-terrestrial networks," 3rd Generation Partnership Project, Technical Report TR 38.811, 2020, release 15.

[42] W. Liu *et al.*, "Effect of turbulence layer height and satellite altitude on tropospheric scintillation on Ka-band Earth–LEO satellite links," *IEEE Transactions on Vehicular Technology*, vol. 59, no. 7, pp. 3181–3192, 2010.

[43] M.-M. Zhao *et al.*, "Intelligent reflecting surface enhanced wireless networks: Two-timescale beamforming optimization," *IEEE Transactions on Wireless Communications*, vol. 20, no. 1, pp. 2–17, 2021.

[44] M. Röper *et al.*, "Position-based transceiver design for multiple satellite to VSAT downlink," *IEEE Open Journal of the Communications Society*, vol. 5, pp. 7022–7040, 2024.

[45] 3GPP, "Part 5: Satellite access radio frequency (RF) and performance requirements," 3rd Generation Partnership Project, Technical Report TR 38.101, 2025, release 19.

[46] H. Lee *et al.*, "Can TDD be employed in LEO SatCom systems? Challenges and potential approaches," *arXiv preprint arXiv: 2502.08179*, 2025.

[47] K. Guo *et al.*, "On the performance of LMS communication with hardware impairments and interference," *IEEE Transactions on Communications*, vol. 67, no. 2, pp. 1490–1505, 2019.

[48] F. Kunzi *et al.*, "Precise onboard time synchronization for LEO satellites," *NAVIGATION: Journal of the Institute of Navigation*, vol. 69, no. 3, 2022.

[49] F. S. Prol *et al.*, "Position, navigation, and timing (PNT) through low earth orbit (LEO) satellites: A survey on current status, challenges, and opportunities," *IEEE Access*, vol. 10, pp. 83 971–84 002, 2022.

[50] J. Zhu *et al.*, "Timing advance estimation in low Earth orbit satellite networks," *IEEE Transactions on Vehicular Technology*, vol. 73, no. 3, pp. 4366–4382, 2024.

[51] Y. Zhang *et al.*, "Privacy preservation in delay-based localization systems: Artificial noise or artificial multipath?" in *GLOBECOM 2024 - 2024 IEEE Global Communications Conference*, 2024, pp. 2755–2760.

[52] C. Ozturk *et al.*, "RIS-aided localization under pixel failures," *IEEE Transactions on Wireless Communications*, vol. 23, no. 8, pp. 8314–8329, 2024.

[53] S. Gezici *et al.*, "Ranging in a single-input multiple-output (SIMO) system," *IEEE Communications Letters*, vol. 12, no. 3, pp. 197–199, 2008.

[54] Y. Zhang *et al.*, "Distance-angle beamforming for covert communications via frequency diverse array: Toward two-dimensional covertness," *IEEE Transactions on Wireless Communications*, vol. 22, no. 12, pp. 8559–8574, 2023.

[55] ——, "Robust transceiver design for covert integrated sensing and communications with imperfect CSI," *IEEE Transactions on Communications*, vol. 73, no. 9, pp. 8016–8031, 2025.

[56] Q. Shi *et al.*, "An iteratively weighted MMSE approach to distributed sum-utility maximization for a MIMO interfering broadcast channel," *IEEE Transactions on Signal Processing*, vol. 59, no. 9, pp. 4331–4340, 2011.

[57] Y. Zhang *et al.*, "Enabling scalable distributed beamforming via networked leo satellites towards 6G," *IEEE Transactions on Wireless Communications*, vol. 25, pp. 6666–6680, 2026.

[58] A. M. Hamza *et al.*, "Interference analysis and mitigation for time-asynchronous OFDM CoMP systems," *IEEE Transactions on Wireless Communications*, vol. 17, no. 7, pp. 4780–4791, 2018.

[59] International Telecommunication Union, "Attenuation by atmospheric gases and related effects," International Telecommunication Union, Geneva, Recommendation P.676-12, 2019.

[60] A. Al-Hourani *et al.*, "On modeling satellite-to-ground path-loss in urban environments," *IEEE Communications Letters*, vol. 25, no. 3, pp. 696–700, 2021.